Title: Unsupervised functional neurocartography of the *Aplysia* buccal ganglion

Authors: Renan M. Costa[1,2,*], Vijay A. Dharmaraj[1,3,*], Ryota Homma[1,*], Curtis L. Neveu[1], William B. Kristan[4], and John H. Byrne[1,2]

*These authors contributed equally to the work.

Author affiliations:

[1]Keck Center for the Neurobiology of Learning and Memory, Department of Neurobiology and Anatomy, McGovern Medical School at The University of Texas Health Science Center at Houston; Houston, United States.

[2]MD Anderson UTHealth Graduate School of Biomedical Sciences; Houston, United States.

[4]Division of Biological Sciences, Neurobiology Section, University of California San Diego; La Jolla, United States.

Correspondence should be addressed to:

John H. Byrne
Department of Neurobiology and Anatomy
McGovern Medical School at The University of Texas Health Science Center at Houston
6431 Fannin Street, Suite MSB 7.046
Houston, TX 77030
Tel: 713-500-5602, Fax: 713-500-6023
E-mail: John.H.Byrne@uth.tmc.edu

Author contributions: Conceptualization: RMC, VAD, RH, CN, JHB. Methodology: RMC, CN, JHB. Investigation: RMC. Data curation: RMC, VAD. Software: RMC, VAD, RH. Visualization: RMC, RH. Analysis: RMC, VAD, RH. Funding acquisition: JHB. Project administration: JHB. Supervision: JHB. Writing—original draft: RMC, VAD, RH. Writing—review & editing: RMC, RH, CN, WBK, JHB.

Acknowledgments: We thank Dr. E. Paxon Frady for assistance with the implementation of the original functional neurocartography framework. This work was supported by National Institutes of Health grant R01 NS101356 (JHB), CNPq Science without Borders Scholarship 203059/2014-0 (RMC), and a Larry Deaven Ph.D. Fellowship in Biomedical Sciences (RMC).

[3] Present address: Michael E. DeBakey Department of Surgery, Baylor College of Medicine; Houston, United States.

ABSTRACT

A major limitation of large-scale neuronal recordings is the difficulty in locating the same neuron in different subjects, referred to as the “correspondence” issue. This issue stems, at least in part, from the lack of a unique feature that unequivocally identifies each neuron. One promising approach to this problem is the functional neurocartography framework developed by Frady et al. (2016), in which neurons are identified by a semi-supervised machine learning algorithm using a combination of multiple selected features. Here, the framework was adapted to the buccal ganglia of *Aplysia.* Multiple features were derived from neuronal activity during motor pattern generation, responses to peripheral nerve stimulation, and the spatial properties of each cell. The feature set was optimized based on its potential usefulness in discriminating neurons from each other, and then used to match putatively homologous neurons across subjects with the functional neurocartography software. A matching method was developed based on a cyclic matching algorithm that allows for unsupervised extraction of groups of neurons, thereby enhancing scalability of the analysis. Cyclic matching was also used to automate the selection of high-quality matches, which allowed for unsupervised implementation of the machine learning algorithm. This study paves the way for investigating the roles of both well-characterized and previously uncharacterized neurons in *Aplysia,* as well as helps to adapt this framework to other systems.

INTRODUCTION

Analyses of the function and connectivity of a neuronal circuit require the ability to identify and characterize the individual functional units within it. In simpler nervous systems, this characterization is facilitated because these nervous systems are known to contain many individually unique neurons (e.g., Byrne, 2019). Conversely, in more complex systems, the functional unit of interest may be a group of similarly-behaving neurons or even an entire region. In either case, the traditional approach has been to distinguish these functional units by using some defining feature or trait (e.g., a protein, gene, metabolite, neurotransmitter, morphology, synaptic connection, or activity pattern). However, in the majority of cases neurons or groups of neurons are not readily identifiable by a signature feature alone. Even when a single feature purportedly identifies a neuron type, future experiments tend to find subcategories of that group (e.g., Abrahao and Lovinger, 2018; Björklund and Dunnett, 2007; Hernández et al., 2015; Mallet et al., 2012; Tiklová et al., 2019). Similarly, functional unit characterization proves problematic when comparing the same circuit between two different subjects. Although investigation *in vitro* may demonstrate two subjects to be physiologically similar, inherent intersubject variability can make identifying even the most obvious homologous functional units between them nontrivial. This problem of intersubject variability is known as the issue of correspondence (Aberg et al., 2009; Hassanien et al., 2009; Yendiki et al., 2016).

To address the issue of correspondence, Frady et al. (2016) developed an analytical framework termed *functional neurocartography*. They built and optimized a rich feature-space composed of several features that were informative for the identification of many individual leech neurons recorded by voltage-sensitive dye (VSD) imaging. Cells were identified algorithmically based on features extracted from neuronal activity during behavior, and putatively homologous neurons were identified through careful curation of the results. Neurons from these experiments were then fit onto a reference map template based on known information from the literature and this mapping process also revealed previously uncharacterized neurons. Although this approach is very useful, it requires the curator to be well informed of the structure and function of the neuronal circuit being

investigated. The present study aimed to generalize neurocartography approaches for nervous systems where such information may not be so readily available.

This study applied the functional neurocartography approach to the neurons in the buccal ganglion of the marine mollusc *Aplysia californica.* The buccal ganglia contain a central pattern generating (CPG) circuit that mediates the consummatory aspects of feeding behavior (for reviews see Baxter and Byrne, 2006; Cropper et al., 2004). The ganglion continues to produce spontaneous buccal motor patterns (BMPs) after removal from the animal and many neurons essential for the generation of BMPs have been characterized (for reviews see Baxter and Byrne, 2006; Cropper et al., 2004). In addition, VSD imaging has been successfully used in large-scale recordings from buccal ganglia neurons (Costa et al., 2021; Morton et al., 1991; Neveu et al., 2017). Although neurons in the buccal ganglion are individually identifiable, the criteria vary considerably. For the majority of neurons, an elaborate combination of anatomical and physiological properties are necessary for identification. And many neurons remain uncharacterized because of their identifying features have yet to be documented. Searches for uncharacterized neurons that contribute to BMPs are still ongoing (e.g., Costa et al 2021; Momohara et al., 2021). Consequently, this model system could benefit greatly from functional neurocartography.

Here, we implemented and expanded the functional neurocartography framework, and used anatomical and physiological neuronal features from multiple experiments to make pairwise comparisons and match neurons between preparations. Several key adaptations were made. First, in addition to the typical VSD imaging of neuronal activity during motor pattern generation, VSD signals were measured from neurons in response to stimulation of different peripheral nerves. This manipulation added a set of robust and distinct features to the feature-space. Second, novel tools were developed for matching neurons across subjects, which used a cyclic matching algorithm (Hofbauer, 2016) to chain together pairs of experiments and form families of neurons. This approach circumvents the problem of integrating pairwise matching results across all animals (termed “stitching” in the functional neurocartography framework) and enables an unsupervised analytical pipeline for the cross-subject matching of homologous neurons.

This automated analytical pipeline will also help enhance the scalability of the framework to accommodate a larger number of subjects. These adaptations and enhancements will facilitate the future use of neurocartography for analyses of the *Aplysia* buccal ganglion, as well as other nervous systems.

RESULTS

Spatial and Functional Features

In order to build an information-rich feature-space, we first collected data on many spatial and functional features of each neuron and assessed the usefulness of each feature. Potential sources of useful information on individual neurons include size and position, characteristics of activation during motor pattern generation, and responses to stimulation of peripheral nerves. This information was acquired by combining population-wide VSD imaging with extracellular nerve recording and stimulation. Here, we provide an overview of the experimental configuration and of the extracted neuronal features. Detailed descriptions are provided in Materials and Methods.

The activity produced by individual neurons in isolated *Aplysia* buccal ganglia during motor pattern generation (Fig. 1) was measured by staining ganglia with VSD RH-155. Suction electrodes were used to record activity in buccal nerves 1–3 (cBn1, cBn2, cBn3, iBn2, iBn3—where *c* and *i* denote whether the nerve was *contralateral* or *ipsilateral* to the imaged hemiganglion), the esophageal nerve 2 (iEn2) and the radular nerve (iRn). Activity in these nerves is correlated with specific phases of the animal's feeding behavior (i.e., protraction, retraction, post-retraction; Cropper et al., 2004; Morton and Chiel, 1993b). The relationship between the activity of individual neurons and these phases, in turn, provides potentially useful information about the behavioral role of each cell (e.g., Morton and Chiel, 1993a). Two sets of experiments were performed: one recording from the caudal (n = 7) surface of the left buccal hemiganglion and the other from the rostral (n = 6) surface.

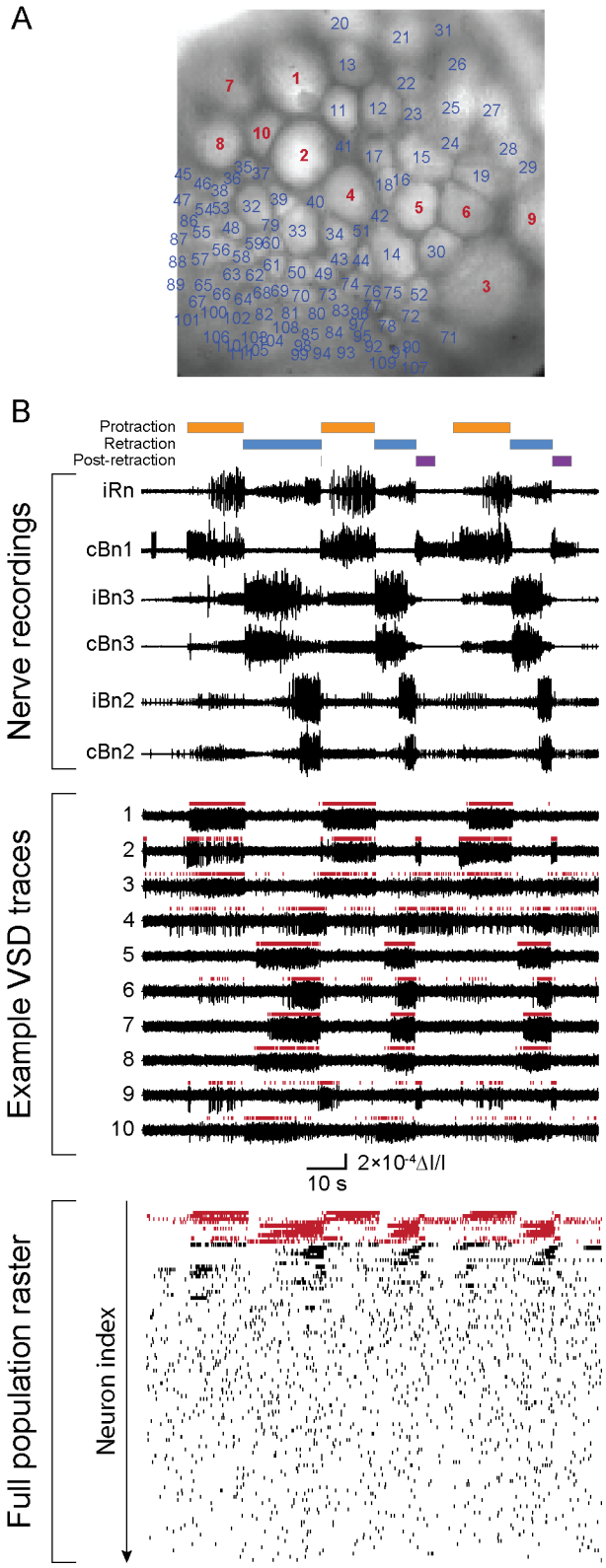

Figure 1. Concurrent voltage-sensitive dye (VSD) imaging and extracellular nerve recordings during motor pattern generation. A. Caudal surface of the buccal ganglion. Example neurons displayed in (B)

are highlighted in red. A total of 111 neurons were in the field of view for this preparation. **B.** (Top) Extracellular nerve recordings were used to monitor motor pattern generation and to identify each phase of a motor pattern (protraction, retraction and post-retraction). (Center) Example VSD traces from 10 neurons during the same period. Vertical red lines above each trace denote the occurrence of action potentials. (Bottom) Raster of the spike trains from all 111 neurons. Neurons displayed as examples above are highlighted in red.

The timing of the spike activity detected from the VSD recordings was examined next (Fig. 1B; see Material and Methods). Many neurons were active predominantly during one or more of the three BMP phases (protraction, retraction, post-retraction). Phase preference was quantified as the normalized activity of a neuron during each phase of the BMP (Fig. 2A). This yielded three *preference* features—one for each BMP phase.

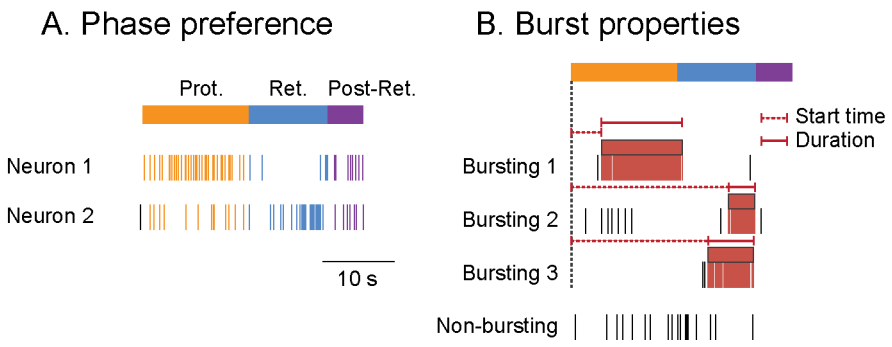

Figure 2. Features of neuronal activity during motor patterns. A. *Preference* of neuron activity for each phase of a motor pattern. Orange box denotes protraction, blue retraction, and purple post-retraction. Spikes that were used to compute a neuron's preference toward a given phase are highlighted in the corresponding color. **B.** Bursts of activity in each spike train were labeled and neurons were classified as either bursting or non-bursting. Red boxes denote bursts identified in each spike train. Spikes in each burst are highlighted in red. The overall level of burst-like activity in each neuron was quantified as the firing rate during bursts. This feature was termed *frequency*. *Start time* was the time elapsed between the onset of a motor pattern and the onset of burst-like activity in each neuron. *Duration* was the total length of bursts for each neuron. See Materials and Methods for details on the quantification of each feature.

Neurons were classified as bursting or non-bursting using previously described criteria (Neveu et al., 2017; see Materials and Methods), which yielded a binary feature termed *bursting*. Additional features were obtained from the burst properties of each *bursting*-positive neuron, including the firing rate during bursts (*frequency*) and the *start time* and *duration* of burst-like activity during BMPs. *Start time* and *duration* were

extracted after normalizing the duration of each phase of a motor pattern, whereas *frequency* was calculated prior to normalization.

Neurons within the buccal ganglia may send processes through one or more peripheral nerves (Evans and Cropper, 1998; McManus et al., 2014; Morton and Chiel, 1993b; Scott et al., 1991), as well as receive synaptic input from cells whose processes pass through these nerves (Nargeot et al., 1999). Nerve stimulation can therefore activate neurons both directly and indirectly, thereby providing a potential rich source of information on many cells. VSD imaging was used to capture the responses of all neurons to stimulation of each of the recorded nerves (Fig. 3). The amplitude of neuronal activity following nerve stimulation yielded seven *nerve response* features, one for each of the seven stimulated nerves (cBn1–3, iBn2–3, iEn2, iRn).

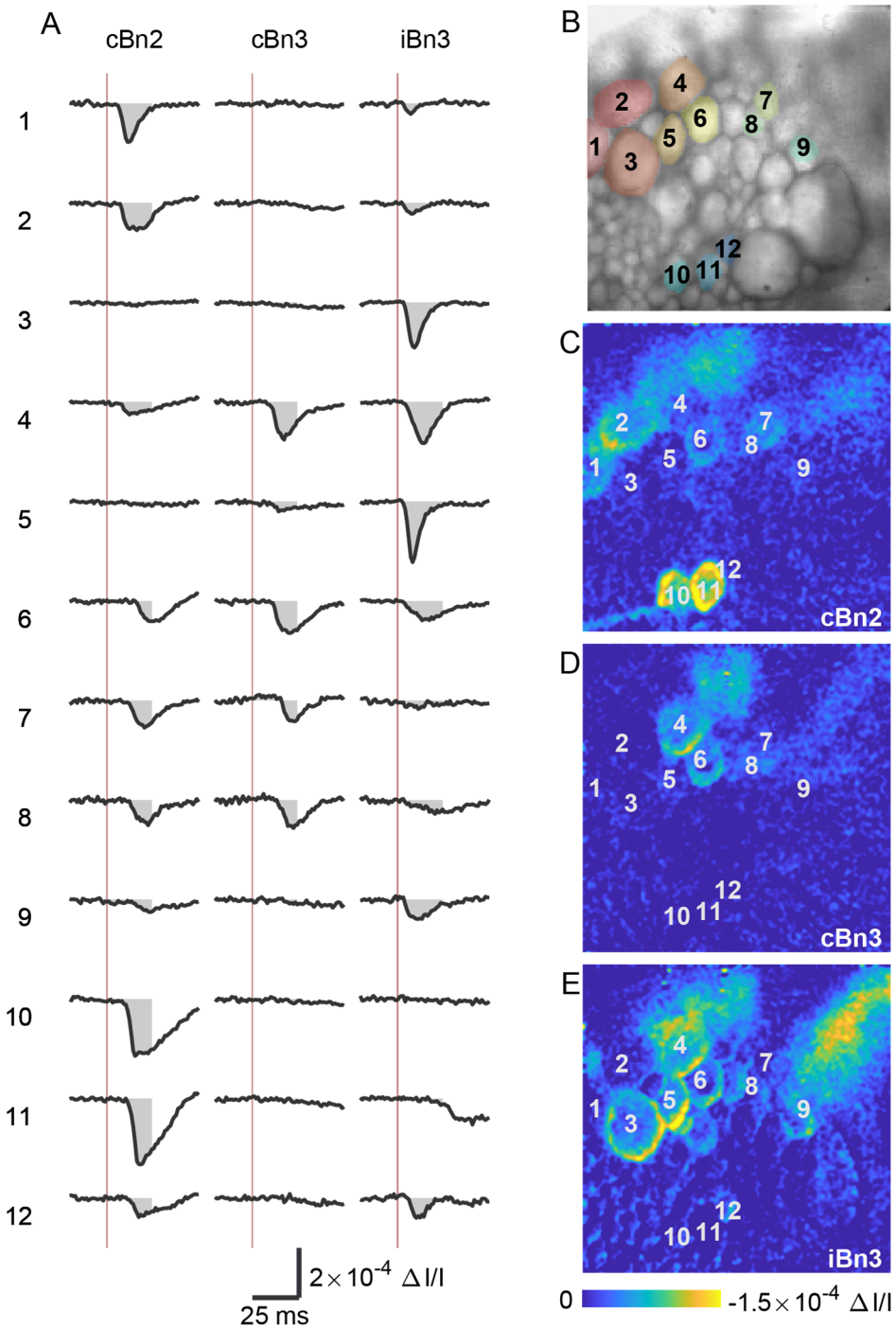

188

189 **Figure 3. Feature extraction from responses to nerve stimulation.** In response to stimulation of
190 individual nerves, distinct subsets of neurons exhibit VSD responses. The *response amplitude* feature was
191 defined as the integral of the trace over the first 25 ms following nerve stimulation (shading). **A.** Example
192 time courses of the VSD signal in response to the nerve stimulations. Note that a downward deflection in
193 the VSD trace corresponds to a depolarization. Responses of 12 neurons to 3 nerves (cBn2, cBn3, and
194 iBn3) are presented. Neuron indexes correspond to the numbers in panels B–E. Each trace is an average

of 40 responses. Red vertical lines indicate the time of nerve stimulation. Gray shading represents the 25 ms time window used to compute the *response amplitude* feature. **B.** Image of the VSD-stained buccal ganglion showing the 12 neurons that generated the recordings in panel A. **C–E.** Activity in response to stimulation of each of the three nerves. The response maps were obtained by subtracting the ΔI/I image of the baseline periods (average over -10–0 ms and 45–55 ms relative to the stimulus onset) from that of the post-stimulus period (average over 45 ms after the stimulus; a larger time window than the 25 ms window for the amplitude parameter was used for improved image quality).

Finally, the spatial features for all imaged neurons were quantified. The ganglion was positioned at approximately the same location across experiments. In addition, variations were accounted for by approximating the orientation and offset of both the ventral cluster and the entire ganglion, and then aligning each recording accordingly, as previously described (Neveu et al., 2017). The centroid of the pixels overlying each neuron was used as the *x* and *y* coordinates for the *position* feature, and the total number of pixels was used to estimate the *size* feature.

Feature Assessment

We next evaluated what subset of features would form the optimal feature-space. The quality of a feature depends primarily on three factors: i) how much information it provides; ii) how much of that information is unique relative to other features (non-redundancy); and iii) the extent of its variability within and across subjects (consistency). Thus, a high-quality feature must offer non-redundant information that is sufficiently consistent to allow neurons to be distinguished from one another.

The quality of the feature-space was quantified using a metric (termed *discriminability index*) that reflects the percentage of neurons that are distinguishable in a certain feature-space (Frady et al., 2016). Briefly, this index asks whether, upon splitting the data in two halves, a given neuron is closer to itself than to other similar neurons in the feature-space. If that is the case, the neuron is deemed discriminable, that is, distinguishable from other neurons. The discriminability index was computed for several possible subsets of features (Fig. 4). By selecting the subset of features that maximizes the number of discriminable neurons, we attempted to optimize the usefulness of our feature-space.

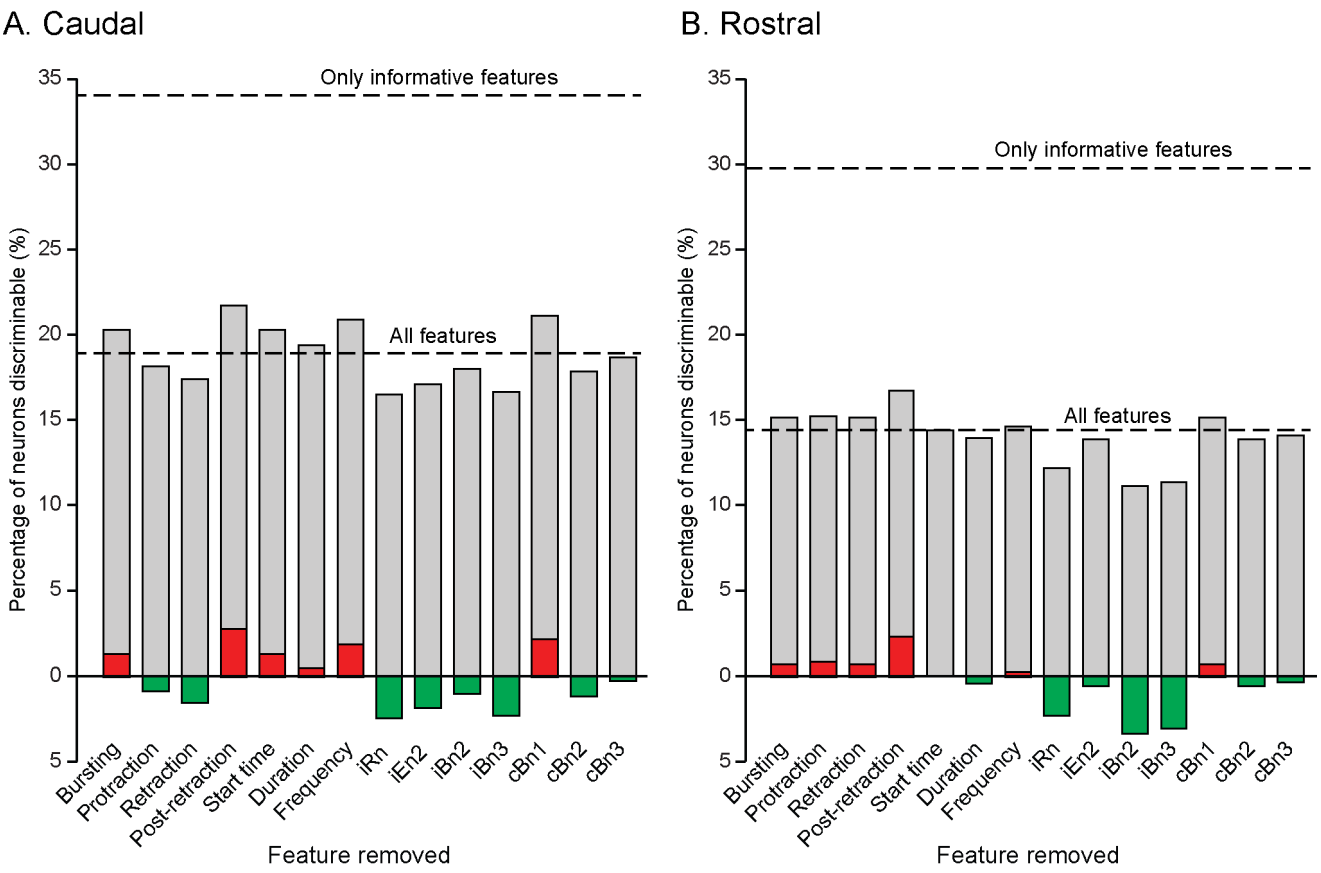

Figure 4. Effect of individual feature removal on neuron discriminability. A. Discriminability of neurons visible from the caudal surface. If a feature contains useful information, removing it must necessarily reduce the ability to discriminate neurons within the subject (green). On the other hand, if removing a feature improves (red) discriminability, it should not be included in the feature-space. **B.** Same as (A), but for neurons visible from the rostral surface.

Feature assessment was performed separately for the rostral and caudal buccal neurons. Two different subsets of features were optimal for the rostral and caudal feature-spaces. For caudal preparations, the selected feature-space consisted of protraction and retraction phase preferences, the start time burst property, and nerve responses for iRn, iBn2, iBn3, cBn2, and cBn3. Conversely, the feature-space for rostral preparations consisted of start time and duration burst properties, in addition to nerve responses for iRn, iBn2, iBn3, cBn2, and cBn3. Responses to iEn2 stimulation were small compared to other nerves, and we could not rule out the possibility that these responses were due to noise. Therefore, we conservatively chose not to include responses to iEn2 stimulation in the final feature-spaces, even though this feature was classified as useful for both caudal

241 and rostral populations by the discriminability analysis and thus potentially contained
242 valuable information. By default, both caudal and rostral spaces included size and
243 position features. The differences between the feature-spaces yielding highest
244 discriminability for each surface imply that certain information may be of greater or lesser
245 value depending on the neuronal population of interest. Specifically, the rostral neurons
246 appeared to rely more on the temporal properties of bursts, while caudal neurons relied
247 more on BMP phase preference. Both, however, were equally reliant on the information
248 contained within the nerve response features. The differences in the optimal subsets of
249 features further substantiated the use of the discriminability index for feature quality
250 assessment and, in addition, highlighted the underlying physiological differences between
251 the rostral and caudal sides of the buccal ganglia.

252 *Pairwise functional neurocartography*

253 The assessment of feature discriminability yielded two libraries of neurons with the
254 feature sets selected for intersubject comparison for the caudal and rostral sets of
255 experiments. Pairwise comparisons of neurons were performed between every unique
256 pair of experiments for each of the caudal and rostral datasets as the first step for
257 identifying homologous neurons across experiments. These pairwise comparisons,
258 performed with the Imaging Computational Microscope (ICM) module of the
259 neurocartography toolset (Frady and Kristan, 2015), generated a metric of neuron-to-
260 neuron match strength, which was based on the extent of similarity across all input
261 features as well as quantity and quality of alternative candidates for the match. The ICM
262 then uses the Hungarian algorithm (Kuhn, 1955) to ensure that as many neurons as
263 possible find matches between experiments by allowing non-best matches. The software
264 is also capable of optimizing the relative contributions of each feature (feature skewing)
265 to manage intersubject variability, which was not utilized at this stage, but was used in
266 subsequent analyses (see the following subsections).

267

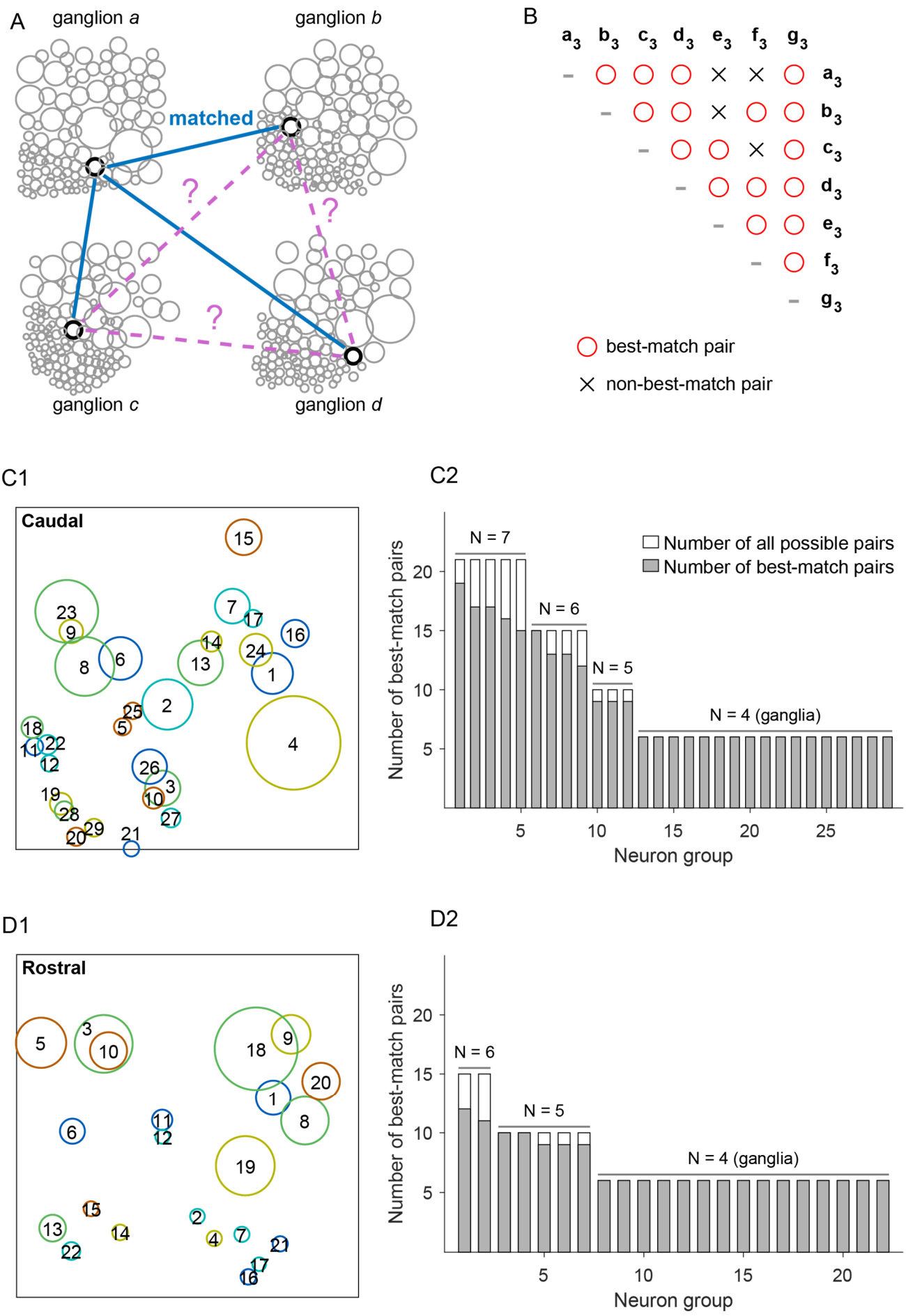
A
ganglion a
ganglion b
ganglion c
ganglion d
matched
?
B
a3 b3 c3 d3 e3 f3 g3
a3
b3
c3
d3
e3
f3
g3
best-match pair
non-best-match pair
C1
Caudal
C2
N = 7
N = 6
N = 5
N = 4 (ganglia)
Number of all possible pairs
Number of best-match pairs
Number of best-match pairs
Neuron group
D1
Rostral
D2
N = 6
N = 5
N = 4 (ganglia)
Number of best-match pairs
Neuron group

Figure 5. Pairwise matching analysis. The Imaging Computational Microscope (ICM; Frady and Kristan, 2015) was used for matching neurons between every pair of experiments based on neurons' similarities in their spatial and functional features. **A.** Matching neurons across ganglia. Although a given neuron in ganglion *a* will be matched with one neuron in each of ganglia *b*, *c*, and *d*, it is not guaranteed that these neurons in b, c, and d will, in turn, be each other's best possible matches when their ganglia are directly compared. As a solution to this problem, neurons were considered to be in a matching group when all neurons were the best match (open circle, B) for each other in all possible pairwise comparisons ("perfect group") among at least four ganglia. **B.** Groups with overlapping neurons were then merged into a single group. The diagram presents such an instance, where letters a_3-g_3 each indicate one neuron in each of the seven separate ganglia. (Specifically, neurons that fell into the group 3 in C.) For example, the four neurons a_3, b_3, c_3, and d_3 form best-match pairs (red circles) a_3-b_3, a_3-c_3, a_3-d_3, b_3-c_3, b_3-d_3, and c_3-d_3. The seven neurons contained eight of such perfect groups (abcd, abcg, abdg, acdg, bcdg, bdfg, cdeg, and defg; subscripts are omitted for clarity) and were merged into a single group. Note that several pairs in the resulting single group are non-best-matches in direct pairwise comparisons (gray crosses). In this example, out of 21 possible pairs between 7 neurons, 17 pairs are best-matches and 4 are non-best. **C1.** All groups of neurons identified through the aforementioned processes from the caudal side. Each circle represents a single group, and the position and size of circle show the median position and size of participating neurons. The colors of circles are for visibility and do not represent specific information. **C2.** The number of participating neurons and number of best-match pairs among them are presented for every group in C. Each bar represents a single group and its position along the X-axis corresponds to the group number in C. **D.** The identified groups from six rostral-side experiments presented in the same format as in C and D. These results are based on the unskewed feature-space (see Figs. 7 and 8).

One drawback of the pairwise approach is that information across all possible pairs needs to be "stitched" (i.e., integrated in some way to obtain unified insights; Frady et al., 2016). Stitching is nontrivial because full consistency of pairwise matches among three or more animals is not guaranteed (Fig. 5A). Frady et al. addressed this issue by training the matching and feature skewing algorithm with human instructions, and then manually curating the results to identify "canonical" neurons that were consistently matched across animals. Although this approach offers the highest possible accuracy, it relies on expertise, and requires substantial human effort. The latter is a limiting factor for the number of animals to which the approach can be applied, as the number of possible pairs of animals is equal to N×(N-1)/2 (i.e., N choose 2), where the N is number of animals. Thus, supervision effort (i.e., the number of matches the analyst has to judge) scales rapidly with the number of animals.

303 Consequently, a more automatic approach for the stitching process was sought.
304 We assessed matches based solely on the consistency of pairwise matching across
305 animals by considering a set of neurons to be successfully matched across subjects when
306 groups of four neurons satisfied the requirement that every possible pair between them
307 are best match neurons in pairwise matching (termed “perfect group”). Four was chosen
308 as the minimum majority of 7 caudal experiments or 6 rostral experiments so that the
309 corresponding neurons cannot appear in two separate sub-groups. Furthermore, when
310 two or more such groups of four neurons shared at least one member neuron, these
311 groups were merged even if there were pairs on non-best match neurons among the
312 groups (Fig. 5B). Before the optimization of intersubject variability, this procedure
313 identified 29 groups in the caudal dataset (Fig. 5C, D) and 22 groups in the rostral dataset
314 (Fig. 5E, F). These numbers are not distant from what is to be expected from the
315 discriminability analysis above, although they are not intended for direct comparison.
316 Among 29 and 22 groups, 12 and 7 groups, respectively, contained five or more member
317 neurons after group merging.

318 *Cyclic matching and copresence analysis*

319 The approach above allows integration of pairwise matches based on the cross-
320 animal consistency of identified groups of neurons, with minimal human effort. However,
321 this solution does not provide an estimate of error, and thus contains little information
322 about the level of confidence in individual identified groups. For example, some of the
323 groups (in particular, those with four members) may be false positives that were matched
324 by chance. In addition, the criterion of perfect groups is possibly too stringent when the
325 number of subjects (and thus its minimum majority) becomes larger, implying another
326 challenge in the scalable automated analysis.

327 To overcome this limitation, we applied a fundamentally different matching
328 strategy, termed *d*-dimensional stable matching with cyclic preferences (cyclic matching;
329 Hofbauer, 2016), in which matching of more than two members can be achieved at once
330 by considering the preference of members in a unidirectional and cyclic manner (Fig. 6A;
331 see Materials and Methods). This cyclic matching algorithm yields complete sets of
332 neurons (referred to as *families*) in the sense that each set contains neurons from all

subjects. But because the matching results generally depend on the unidirectional order of experiments chosen to compute cyclic preferences, cyclic matching was performed repeatedly using randomly shuffled orders of experiments and assessed the robustness of resulting matches based on their consistency across runs (Fig. 6B). With the results of 100 runs of cyclic matching, we assessed the number of times a pair of neurons was present in the same family (referred to as *copresence count*). The copresence counts collectively form a set of copresence profiles for each neuron, which is referred to as reference neuron (Fig. 6B). When a specific neuron exhibits a high copresence count with respect to the reference neuron, they are considered a strong match. When two neurons in the same subject show comparable copresence counts, or when none of the neurons have a salient copresence count, the matching counterpart is uncertain. Conducting this analysis for every neuron in the dataset as the reference neuron, we were able to identify putatively matching pairs of neurons with their copresence count, a metric for the strength of that match and is used in the subsequent analyses.

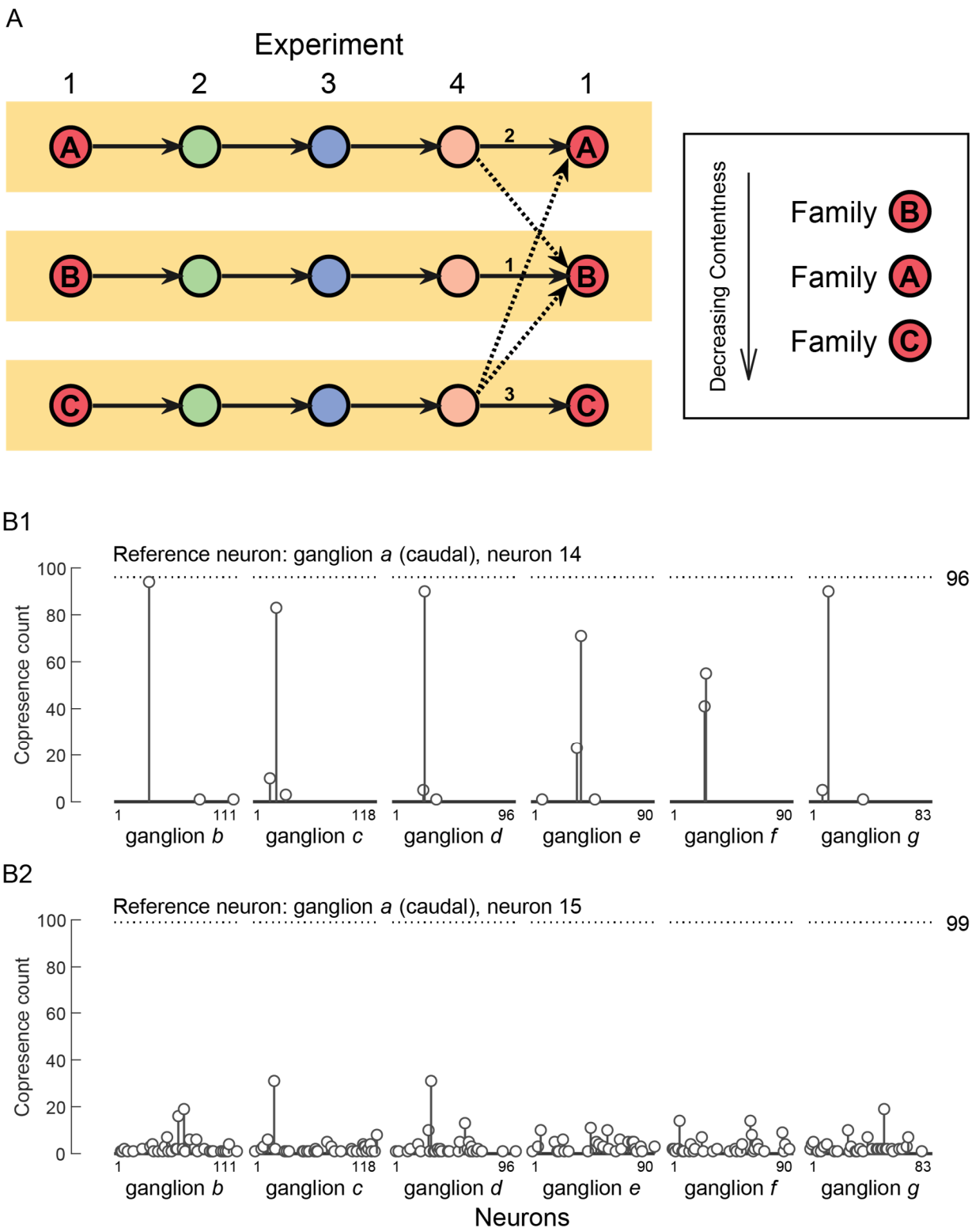

Figure 6. Cyclic matching and copresence analysis. A. Schematic diagram presenting the concept of cyclic matching algorithm. It relies on sequential pairwise matches generated by the Hungarian algorithm, and then assesses the preference of the last cell to the first cell of the same "family" as the rank of their

similarity among the similarity between the last cell and all cells in the first experiment. The family with highest preference is removed from the dataset as an established family. The process is repeated until all cells (in the experiment with fewest cells) form a family. The order of experiments for matching can be arbitrary and matching results are not identical when the orders of experiments are different. **B.** The robustness of individual matchings was determined by performing the cyclic matching process many times (100 cycles) with randomly permuted orders of experiments. A specific neuron (neuron numbers form the x axis) was picked as the reference and for every neuron from other experiments (to be matched), the number of cycles was counted in which the neuron being probed and the reference neuron belonged to the same family ("copresence"). Two examples of such an analysis are presented in two sets of stem plots. **B1,** the reference neuron was picked from ganglion *a* (see Fig. 5). There are six stem plots each of which corresponds to one of ganglia b – g, and each stem represents a single neuron that has a non-zero copresence count. Although a single neuron appeared in the vast majority of runs exclusively in ganglia b, c, d, and g, there were two competing neurons in ganglia e and f, suggesting a failure to find a reliable counterpart. **B2**, the reference was another neuron from ganglion *a*. In this example, there were many candidate neurons in all ganglia, implying that matching is unstable across runs. The same analysis was conducted for every neuron from every experiment, and a pair of neurons is considered as a reliable match when they reciprocally demonstrate highly exclusive copresence. The horizontal dashed line and number in the right indicates the number of cycles (out of 100) the reference neurons appeared in the results.

Feature skewing for the optimization of intersubject comparisons

In our automation-oriented approaches of either pairwise matching or cyclic matching, one key component of the original neurocartography framework was left unused. The ICM software has the capability of optimizing intersubject comparisons through skewing of the feature-spaces of individual subjects. Feature-space skewing is designed to minimize the distances among a set of selected matches, which are deemed "correct." In so doing, skewing emphasizes features that are informative for the correct matches,and minimizes the impact of overall intersubject variability by de-emphasizing less informative features. But to implement skewing, it is necessary to have data on which matches should be selected as correct. Although such data was provided manually by the analyst in the original framework, the copresence results provide that instruction data in the present study. As the high copresence count implies highly consistent matching results across different runs of cyclic matching, it was considered as a proxy of the reliability and used to label the match as correct or not for this analysis.

Selected matches were determined using a copresence proportion criterion, computed over 100 repetitions of cyclic matching. For each match, the copresence proportion was the copresence count of the match (e.g., stems in Fig. 6B) divided by the appearances of the seed neuron (e.g., dashed lines in Fig. 6B). Matches that exceeded a given copresence proportion threshold were selected as “correct” for feature-space skewing. We compared various skewed and unskewed feature-spaces by using the sparseness of the full copresence profile of each reference neuron as an overall quality metric. Neurons whose matches are highly random across runs are expected to have low sparseness, whereas neurons that have consistent matches will have sparse copresence profiles. The sparseness is high when the copresence counts converge to one or just a few neurons, and is low when copresence counts distribute broadly among many neurons. Thus, if skewing results in copresence profiles that converge to fewer neurons, it increases the overall sparseness and improves the feature-space relative to intersubject variability. The ratio of the ℓ_2 norm to the ℓ_1 norm was chosen as the sparseness metric. Both norms are widely used to quantify sparseness, and the ratio between them is a convenient metric due to its scale-invariance (Krishnan et al., 2011; Yin et al., 2014).

A range of copresence proportion thresholds was explored. In caudal preparations, a threshold value of 0.3 yielded the highest overall sparseness (Fig. 7A), the highest number of cells showing a large change (>2.5 times the standard deviation) in sparseness (Fig. 7B) and led to smaller increases in sparseness in many other cells (Fig. 7C). The same threshold also had a similar performance on rostral preparations (Fig. 7D–E). Upon examining the copresence profiles of individual neurons before and after skewing (Fig. 7G–H), we found that many cells that were ambiguously matched across multiple runs in the unskewed feature-space converged more consistently onto the same matches after skewing. These results suggest that skewing to favor matches that are consistent across multiple cyclic runs can improve the feature-space. Thus, a copresence proportion threshold value of 0.3 was used for subsequent analyses of both caudal and rostral preparations.

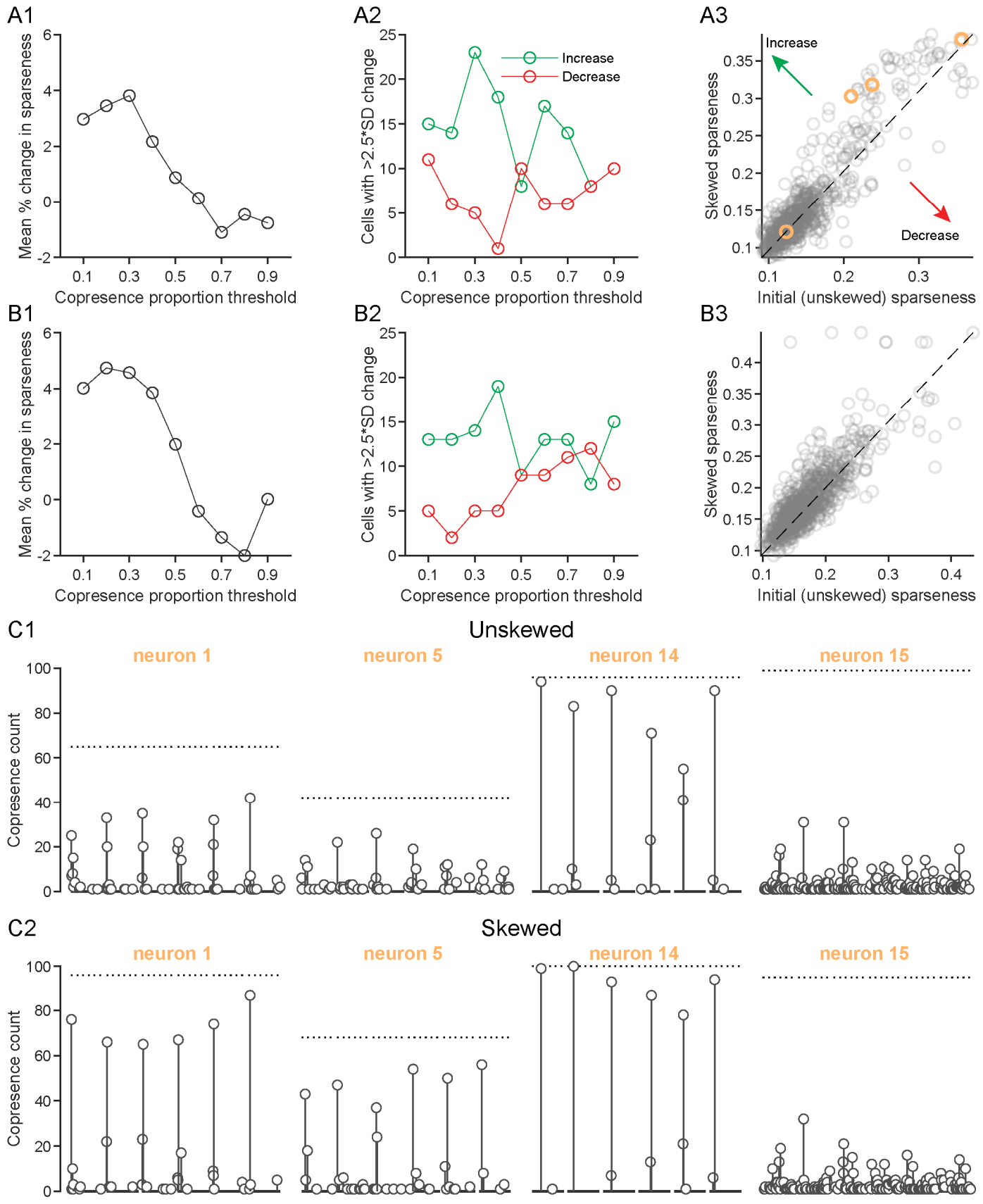
A1
Mean % change in sparseness
Copresence proportion threshold
A2
Cells with >2.5*SD change
Increase
Decrease
Copresence proportion threshold
A3
Skewed sparseness
Increase
Decrease
Initial (unskewed) sparseness
B1
Mean % change in sparseness
Copresence proportion threshold
B2
Cells with >2.5*SD change
Copresence proportion threshold
B3
Skewed sparseness
Initial (unskewed) sparseness
C1
Unskewed
neuron 1
neuron 5
neuron 14
neuron 15
Copresence count
C2
Skewed
neuron 1
neuron 5
neuron 14
neuron 15
Copresence count

412

Figure 7. Feature-space skewing using the cyclic matching copresence criterion. A subset of cross-preparation cell matches was automatically selected for skewing of the feature-space. Matches were included if they met a copresence criterion threshold. **A1.** Overall change in sparseness of the copresence profiles over a range of copresence criterion thresholds. Averaged across all cells from caudal preparations. The threshold value of 0.3 had the largest overall improvement in sparseness. **A2.** Total number of cells displaying a significant increase or decrease in sparseness for each threshold. **A3.** Sparseness of the copresence profile of individual neurons before and after skewing of the feature-space using the 0.3 threshold value. Neurons above the diagonal display increased sparseness after skewing, whereas those below display decreased sparseness. Cells highlighted in orange correspond to examples in panels C1 and C2. **B.** Same as A, but for rostral preparations. **C1.** Copresence profiles of four example reference neurons from caudal preparations with no skewing of the feature-space. Copresence profiles follow the same scheme and seed ganglion as Fig. 6. Note that plots are horizontally compressed to show all target ganglia for each neuron. **C2.** Copresence profiles of the same reference neurons after skewing of the feature-space using the 0.3 copresence criterion threshold.

Groups of putatively homologous neurons based on cyclic matching and comparison with pairwise matching

We next compiled the results of cyclic matching to search for groups of putatively homologous neurons. To achieve this, we first extracted reliable pairs of matching neurons. Reliable pairs were determined based on the uniqueness (exclusiveness) of the copresence count in the copresence profile of a given experiment and a given reference neuron. We defined the uniqueness index (UI) (see Material and Methods), which takes values between 0 and 1 for neurons with highest copresence counts, and values between -1 and 0 for any other neuron. Higher values of UI indicate higher degrees of uniqueness. When a given neuron takes all copresence count in the experiment (i.e., completely exclusive), UI is equal to one, and when two neurons share the same highest count, their UIs are equal to zero, for example. A pair of neurons were considered as reliably matched when they reciprocally had a UI above 0.5 (see Material and Methods). Finally, reliable pairs that shared the same neurons were agglomerated to form a neuron group. In the cases in which the resulting groups included two neurons from the same subject, both neurons were eliminated from the group. Groups with four or more member neurons were

kept for further analyses, although it was technically possible to identify groups of fewer member neurons.

The above process was applied to the cyclic matching results obtained after feature skewing. Nineteen groups from the caudal dataset (Fig. 8A–D), and 22 groups from the rostral dataset (Fig. 8E–F) were identified. For comparison, the cross-animal comparisons of pairwise matches using the feature-skewed datasets was repeated, which yielded 35 and 18 groups in caudal and rostral datasets, respectively.

To compare cyclic groups and pairwise groups, we counted groups that had identical member neurons, as well as those that were not identical, but still shared four or more members. In the caudal dataset, there were five identical groups and six groups with 4+ shared members (Fig. 8A, C). The same analysis was performed using the dataset without feature skewing and obtained one identical group and seven groups with 4+ shared members (Fig. 8D). Note that no seven-member groups were obtained from cyclic matching with the unskewed data. The same comparison of group members was conducted in the rostral dataset (with feature-skewed data), which resulted in four identical groups and three groups with 4+ shared members (Fig. 8E). In addition, the uniqueness index of the group was calculated, which is defined as the mean uniqueness index calculated across all possible pairs (bidirectional) among member neurons in the group (Fig. 8A, B, F). Although the group uniqueness indexes remain relatively high in the cyclic matching groups, which was expected because the grouping process had set a threshold for uniqueness index, the indexes distributed more broadly in the pairwise matching groups. This difference might reflect the lack of a means for quality control in the cross-animal comparisons of pairwise matching.

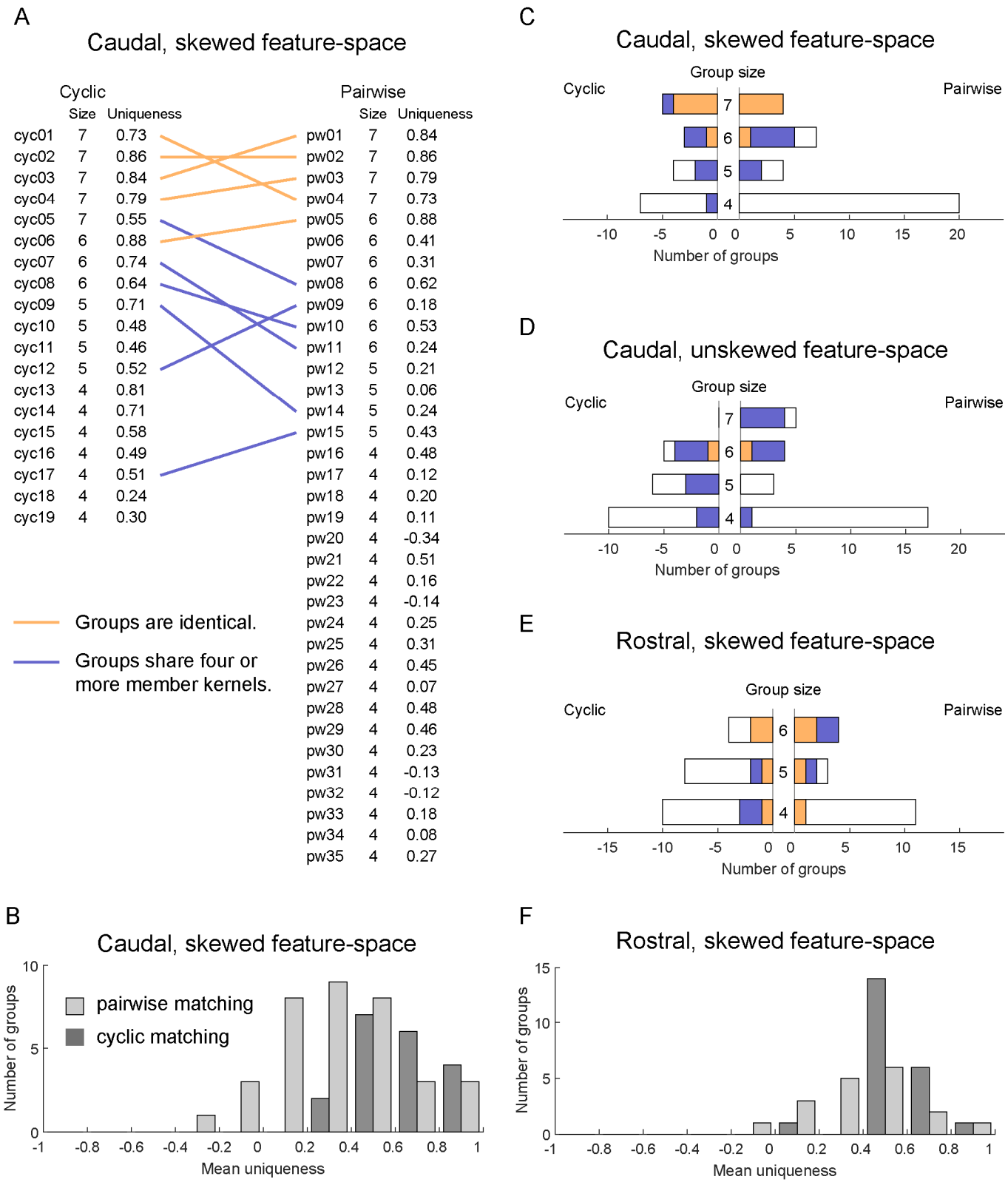

Figure 8. Assembly of the groups of putatively corresponding neurons based on cyclic matching and optimized feature-space. By compiling the information of neuron pairs that showed highly exclusive

copresence from the results of cyclic matching (see text), groups of putatively corresponding neurons are identified. These groups are compared with the groups based on the cross-animal comparison of pairwise matching results, which were also updated from the ones presented in Fig. 5 using the optimized feature-space. **A.** Direct comparison of groups from cyclic matching and pairwise matching about the caudal dataset. Left and right rows list the neuron groups based on cyclic (cyc) matching and pairwise (pw) matching, respectively, with the number of member neurons and mean uniqueness index (a possible metric of matching quality). Groups connected with an orange line are identical in their member neurons. Groups connected with blue lines share four or more member neurons but also contain inconsistent neuron(s) in one or both of groups. **B.** Distribution of the mean uniqueness index of groups presented as histograms. **C.** Number of established groups as well as fully or partially consistent groups between cyclic and pairwise matching in panel A are summarized. **D.** The summary data of group numbers based on unskewed feature set. Note that there is no group with all seven experiments in cyclic matching (left side), resulting in fewer fully consistent groups compared to C. **E, F.** The summary of group numbers and histograms of uniqueness index about rostral dataset. The format of graphs is the same as panels C and B, respectively.

The features of the putatively homologous neurons identified through cyclic matching for caudal and rostral preparations were examined next. Homologous caudal neurons ranged from small to large, but most appeared to be on the larger end (Fig. 9A). Despite substantial variability in the exact position of individual neurons, several patterns can be noted. For example, neuron cyc05 (yellow, Fig. 9) was consistently located on the top left quadrant, often next to or near neurons cyc04 (magenta) and cyc08 (brown). Neurons such as cyc02 (green) and cyc15 (purple) tended to have small to medium sizes, and were located near the border between larger cells and smaller cells. The median features displayed by each putatively identified neuron (Fig. 9B) suggest that most neurons do not possess an individual feature that uniquely identifies them in this feature-space. Rather, most neurons display a unique combination of many features. For example, even though neurons cyc10 and cyc11 are small cells among many other small neurons (e.g., ganglia d–g in Fig. 9A), and share many features they can often be identified due to their unique combinations of features (Fig. 9B). This also appears to be the case for many neurons from the rostral surface (Fig. 10A, B), where most putatively identified cells were small neurons that were responsive to stimulation of many nerves. Similar to caudal neurons, patterns were clear in many putatively identified rostral neurons, such as the sizes and positions of cyc03, cyc04, cyc06, cyc14, and cyc16 (Fig. 10). Taken together, these findings suggest that unsupervised functional

504 neurocartography of the *Aplysia* buccal ganglion can overcome intersubject variability and
505 consistently identify putatively homologous units across animals.

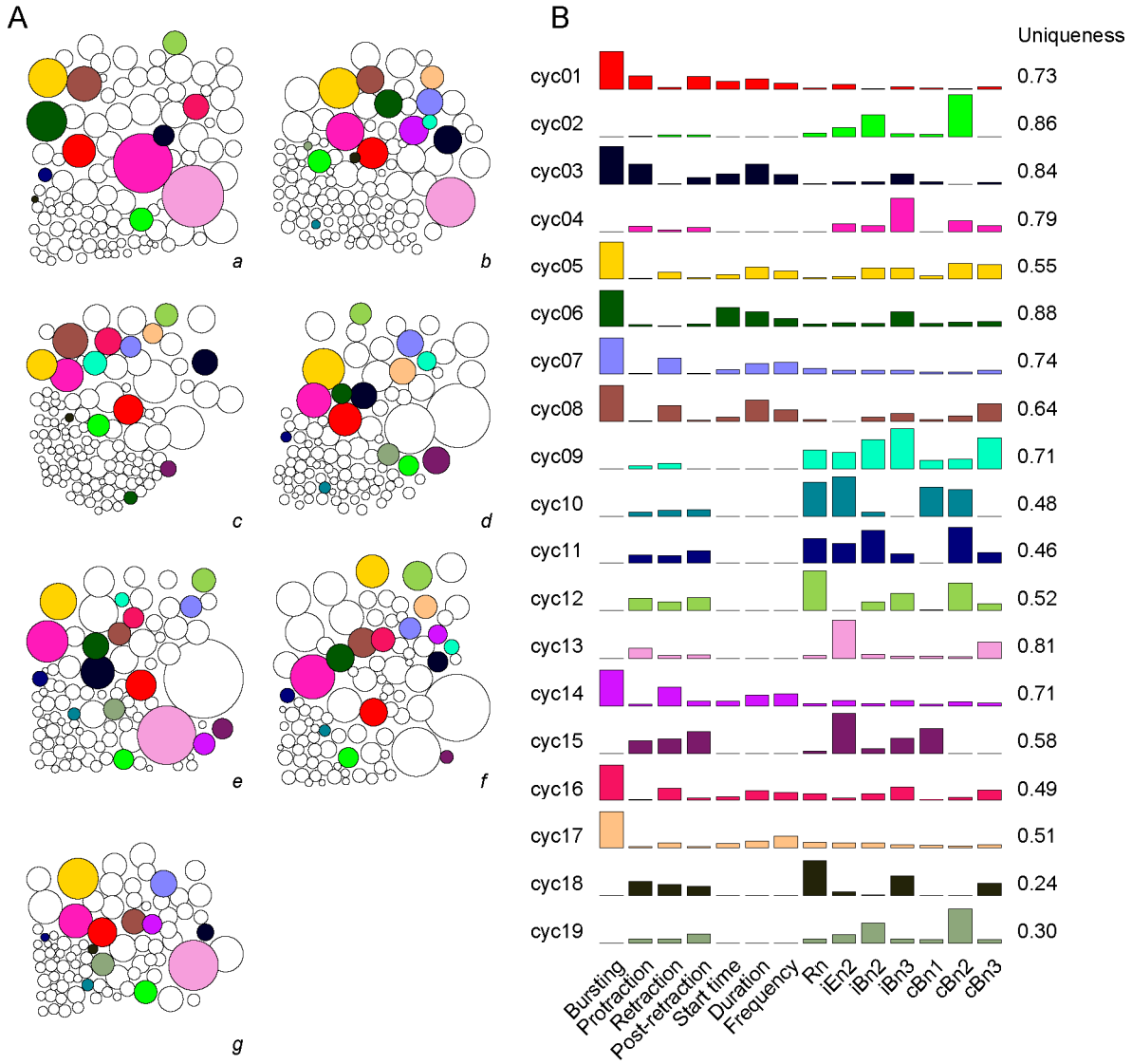

506

507 **Figure 9. Overview of putatively homologous neurons across seven caudal preparations. A.**
508 Diagrams representing the sizes and positions of individual neurons recorded in each caudal preparation
509 (*a*–*g*). Filled circles indicate putatively corresponding neurons, with each color denoting one individual
510 group. For example, the yellow circle (cyc05) usually located on the upper left quadrant of each preparation
511 indicates a neuron that was putatively identified in all seven ganglia. Note that, although many neurons
512 exhibit roughly consistent localization across ganglia, there is substantial variability in the exact position of
513 each cell. **B.** Overall feature profiles of each group. For each feature, the median value across all members
514 of a group is displayed. The y-axis for each feature (i.e., column) is normalized to the maximum observed

515 value of that feature across all caudal neurons. Color scheme corresponds to neurons in panel A. Group
516 labels (cyc01–19) correspond to those in Fig. 8A.

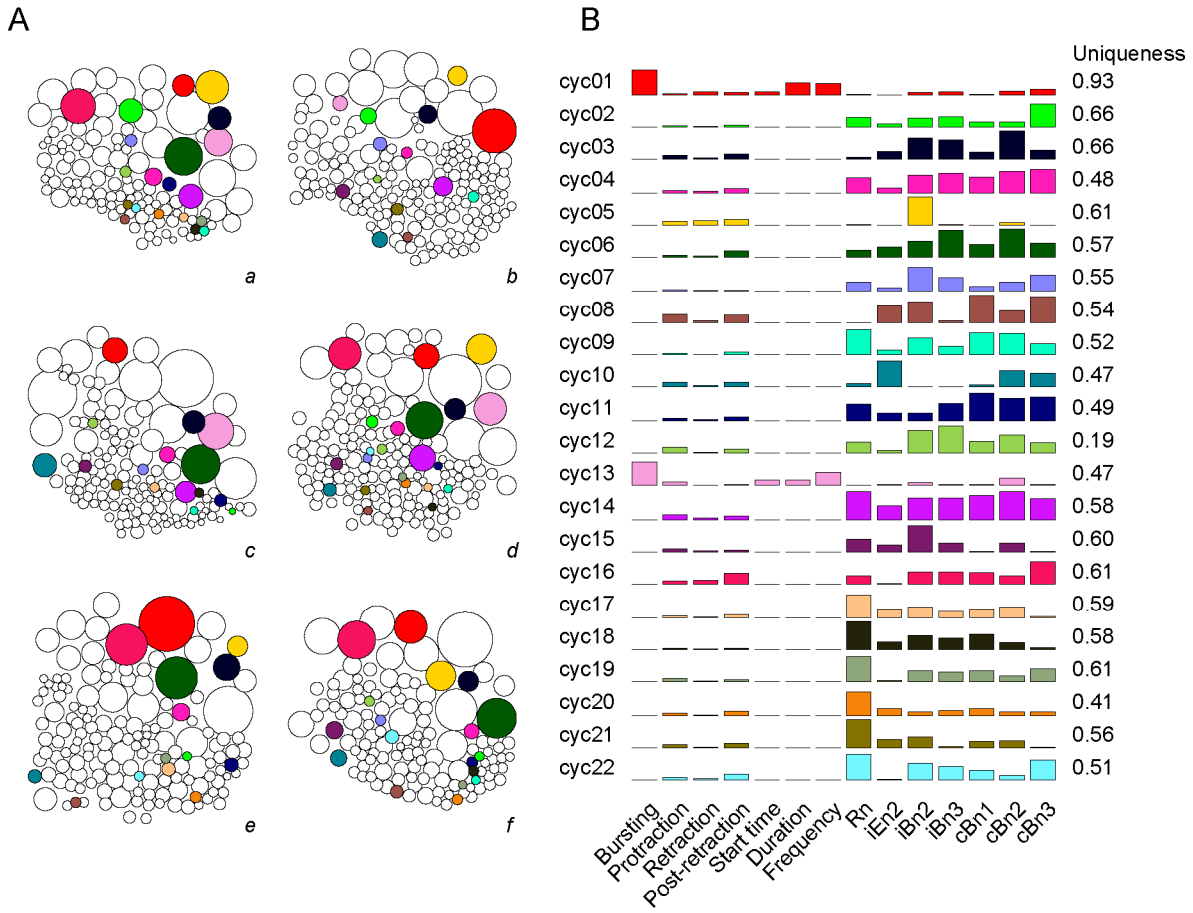

517

518 **Figure 10. Overview of putatively homologous neurons across six rostral preparations.** Same as
519 Figure 9, but for rostral preparations. **A.** Diagrams representing the sizes and positions of individual neurons
520 recorded in each rostral preparation (*a*–*f*). **B.** Overall feature profiles of each group.

521

522 **DISCUSSION**

523 *Functional neurocartography of the* Aplysia *buccal ganglion*

524 The present study applied the functional neurocartography framework (Frady et
525 al., 2016) to the buccal ganglion of *Aplysia* and made several key modifications to
526 enhance its scalability. Neurocartography is composed of two central parts: i) construction
527 of the feature-space, and ii) intersubject matching of neurons based on that feature-
528 space. Each of these is discussed in the following paragraphs.

529 *Developing the feature space for the buccal ganglion*

530 The original framework of neurocartography was developed using VSD imaging
531 data from the leech ganglion. Even though the framework itself is highly versatile, many
532 functional features are specific to each system. Therefore, the first step of our analysis
533 was establishing the feature-space for the buccal ganglion that contained the optimal set
534 of features. The automated algorithm selected parameters related to BMPs. This is not
535 surprising given that many neurons in the buccal ganglion have been characterized based
536 on their activity during BMPs (Baxter and Byrne, 2006; Cropper et al., 2004; Elliot and
537 Susswein, 2002; Jing and Weiss, 2005; Morton and Chiel, 1993b). In addition to purely
538 functional features, the VSD signals evoked in response to the stimulation of different
539 nerves (Fig. 3) were used, which aided discrimination of neurons. Feature selection based
540 on intrasubject variability (Fig. 4) demonstrated that stimulation of various nerves
541 provided useful information in both caudal and rostral datasets. In contrast, some features
542 that were useful for the caudal surface were not useful for the rostral dataset (e.g.,
543 protraction and retraction). This was surprising given that the phasing of neurons has
544 historically been an important defining feature for neurons in the buccal ganglia. Although
545 features related to neuron phasing are known to contain important information, one
546 possibility is that, for the purpose of large-scale neuron discrimination, the information
547 these features bore was redundant with information provided by other features. In that
548 case, it would be beneficial for the overall matching to discard such a redundant feature,
549 even when it is both information-rich and salient to experimenters. These results suggest
550 the need to carefully identify and evaluate the feature sets that are optimally informative
551 for each neuronal population of interest.

Unsupervised pipeline for matching of putatively homologous neurons across subjects

Our primary goal was to increase the degree of automation, thereby enhancing scalability. The original framework (Frady et al., 2016) was designed to utilize human instruction to manage intersubject variability through skewing of the feature-space. In addition, it relied on manual processing to “stitch” the collection of pairwise matching results into groups of putatively homologous neurons. Importantly, this process is nontrivial because pairwise matches are not always consistent if more than two animals are considered.

A key tool in our approach was cross-animal matching based on cyclic matching (Hofbauer, 2016). Although cyclic matching can avoid the problem of inconsistency across pairwise matches, its matching results are generally sensitive to the order of experiments (subjects). Notwithstanding, cyclic matching can be run with many randomly permuted orders of experiments. This strategy makes it possible to discriminate between neuron pairs that are consistently matched across permutations and those that are not (copresence analysis; Fig. 6B).

The parametrization of individual neuron pairs opened a path to the automation of feature-skewing (Fig. 7), allowing for the entire analytic pipeline, including matching putatively homologous neurons, to be automated and unsupervised. Thus, the combination of cyclic matching with the copresence analysis is a promising scalable approach for functional neurocartography. It should be noted, however, that this approach would not work well when the number of subjects is small because of the limitation in the number of possible random permutations. In principle, the ability to estimate intersubject variability is dependent upon the number of subjects from which the estimation is performed. Thus, it is to be expected that a reduced number of animals should impair performance of any approach that needs to estimate intersubject variability.

Limitations and further improvements

Several aspects of the approach may be improved in future studies. First, inclusion of additional informative features would increase the number of identifiable neurons. Many neurons were not responsive to nerve stimulation, did not display characteristic activity

during BMPs, and often had similar spatial features; thus, there was little information available to differentiate these cells. Therefore, one direct means to increase the number of identifiable homologous neurons would be to uncover additional features that are particularly informative for this population. Possible features to be examined include: i) response to stimulation of other nerves or connectives (e.g., i/cEn1, cEn2, i/c salivary nerves, i/c I2 nerves, cRn, iBn1, i/c cerebral-buccal connectives); ii) activity responses to various chemical manipulations (e.g., ionic concentrations of the artificial seawater bath solution, small molecule neurotransmitters, neuropeptides, receptor agonists and/or antagonists); iii) immunostaining for specific transcripts (e.g., neurotransmitters, neuropeptides, receptors, kinases, etc.); and iv) patterns of synaptic connectivity.

Second, a reduction in the sparseness of the current features could be beneficial. The feature set in this study includes a larger number of features than Frady et al. (2016) and, more importantly, those individual features appeared to be sparser. This may have made the matching analysis more prone to measurement noise and compromised the accuracy of matching, especially in neurons with relatively few prominent features. To further improve matching accuracy by increasing robustness to noise, the most straightforward approach would be to examine whether simple dimensionality reduction techniques (e.g., principal component analysis) would effectively reduce the number of features without losing critical information, thereby reducing feature sparseness.

Third, estimates of intersubject variability may be useful for feature selection. In both the original framework and in the present study, feature selection was based on the *intra*subject variability of feature data. This is purely due to the lack of tools to evaluate features based on their *inter*subject variability, as intersubject variability is more directly relevant to intersubject matching of neurons. The automated matching procedure developed in this study could allow for the optimization of features based on their intersubject variability if various subsets of features were directly fed to the matching pipeline. Although the metrics for evaluating the overall performance of matching results are still limited, this strategy could simplify and improve the process of feature selection.

Finally, the analytical pipeline may be further refined through its application to a dataset for which the ground-truth is known. We had limited means to assess the

accuracy of matching results, primarily due to the lack of ground-truth data. Although there is no experimental technique existing to generate such large-scale ground-truth data, the use of simulated data (e.g., noise-added versions of real data) may be helpful in assessing the performance of the analytical pipeline. Furthermore, experiments could be designed to validate a small subset of the results by performing intracellular recordings following the imaging, similar to Frady et al. (2016), given that many neurons in the buccal ganglion have been electrophysiologically and morphologically identified (e.g., Church et al., 1991; Dembrow et al., 2003; Gardner, 1971; Kabotyanski et al., 1998; Plummer and Kirk, 1990; Susswein and Byrne, 1988). An ultimate goal in the neurocartography of the *Aplysia* buccal ganglion would be to associate the groups of homologous neurons with neurons that were previously characterized in the literature. Such an effort may lead to groups of homologous neurons with no previously identified counterpart, i.e., groups of yet uncharacterized neurons, and ultimately to a thorough canonical map of the *Aplysia* buccal ganglion.

626 **MATERIALS AND METHODS**

627 Experimental methods in this study closely follow those described in Costa et al.
628 (2021).

629 *Animals and preparations*

630 *Aplysia californica* were obtained from South Coast Bio-Marine LLC (San Pedro,
631 CA) or bred at the National Resource for *Aplysia* of the University of Miami (Miami, FL).
632 Data were collected from a total of 13 animals weighing between 25 and 50 g. Prior to
633 dissection, animals were injected with a volume of isotonic $MgCl_2$ equal in milliliters to
634 50% of the animals' mass in grams. The buccal mass with buccal ganglia attached was
635 isolated from the animal and placed in a Sylgard-coated chamber containing artificial
636 seawater with a high concentration of divalent cations (HiDi-ASW; 210 mM NaCl, 10 mM
637 KCl, 33 mM $CaCl_2$, 145 mM $MgCl_2$, 20 mM $MgSO_4$, 10 mM HEPES, pH adjusted to 7.5
638 with NaOH). HiDi-ASW was used to reduce activity and muscle contractions during
639 dissection. Buccal ganglia with buccal nerves were excised from the buccal mass and
640 pinned down. The sheath of connective tissue around the ganglia was kept intact. Bipolar
641 suction electrodes for recording and stimulation were positioned on each nerve (see
642 below). HiDi-ASW was substituted with normal artificial seawater (ASW; 450 mM NaCl,
643 10 mM KCl, 10 mM $CaCl_2$, 30 mM $MgCl_2$, 20 mM $MgSO_4$, 10 mM HEPES, pH adjusted
644 to 7.5 with NaOH) prior to recording. Preparations were maintained at 15 °C throughout
645 the experiment.

646 *Extracellular electrophysiology*

647 Bipolar suction electrodes were used to monitor nerve activity associated with
648 buccal motor patterns (BMPs). Nerve signals were amplified by A-M Systems model 1700
649 differential AC amplifiers and digitized by Axon Instruments Digidata 1322A at 20 kHz.
650 The following nerves were recorded: the ipsilateral and contralateral buccal nerves 2 and
651 3 (iBn2, cBn2, iBn3, cBn3); contralateral buccal nerve 1 (cBn1); ipsilateral radula nerve
652 (iRn); and ipsilateral esophageal nerve 2 (iEn2).

653 The responses of the neurons in the imaged hemiganglion to brief electric shocks
654 to the peripheral nerves of the ganglion were characterized; a procedure designed to

655 activate neurons directly if a particular neuron had an axonal projection in the stimulated
656 nerve, or indirectly via synaptic drive from other neurons, or a combination of the two.
657 This procedure was repeated over 40 trials for each of the nerves (i.e., iBn2, iBn3, iEn2,
658 iRn, cBn1, cBn2, cBn3). Stimulation was automatically triggered by a WPI Pulsemaster
659 A300 and delivered by a WPI 850A stimulus isolator. Stimulus intensity, pulse duration
660 and frequency were respectively 15 V, 0.5 ms, 2 Hz for caudal and 30 V, 1 ms, 2 Hz for
661 rostral preparations. Both types of stimulation were effective in eliciting responses and
662 produced informative features.

663 BMPs were manually identified from nerve activity. Activity in Bn1 was used as an
664 indicator of the timing of each BMP phase. Bn1 is particularly informative because it is
665 active during protraction, inactive during retraction, and active again upon retraction
666 termination. A BMP was identified when three criteria were met: (1) large-unit activity
667 lasting at least 3 s occurred in Bn1; (2) the Bn1 activity was followed by large-unit activity
668 in at least one of the two Bn3s; (3) large-unit Rn activity occurred during either the Bn1
669 activity (protraction) or the subsequent Bn1 suppression (retraction). Large-unit activity
670 was defined as all activity with amplitude above a voltage threshold for each nerve, which
671 was set independently for each experiment. The threshold for Bn1 was set to include all
672 units that were consistently active during protraction and inactive during retraction. The
673 Bn3 threshold was set to include only the largest units, which correspond to B4, a neuron
674 known to be active at the onset of retraction. Large-unit activity was counted when at least
675 3 spikes occurred with interspike intervals ≤4 s.

676 *Voltage-sensitive dye (VSD) imaging*

677 Isolated buccal ganglia were stained for 7 min with 0.2 mg/ml of the absorbance
678 VSD RH-155 (TRC Canada) in ASW. After staining, the solution was swapped for a lower
679 concentration of RH-155 in ASW (0.01 mg/ml), which was kept for the remainder of the
680 experiment. Using a Gilson Minipuls 3 peristaltic pump, the solution was continuously
681 cycled through a Warner Instruments SC-20 inline cooler/heater under control of a
682 Warner Instruments CL-100 temperature controller, which maintained the preparation at
683 15 °C. Imaging data was acquired by a Deep Well NeuroCMOS 128×128 camera
684 (RedShirtImaging, SciMeasure) sampled at 1 kHz. The camera was fitted to an Olympus

685 BX50WI microscope equipped with an Olympus 20× 0.95 NA XLUMPlanFL water
686 immersion objective lens. The preparation was illuminated with a 150 W, 24 V Osram
687 halogen light bulb powered by a Kepco ATE 75-8M power supply. Before reaching the
688 preparation, light passed through a Brightline 710/40 nm bandpass filter.

689 Preparations were imaged during BMP generation for two separate 120 s time
690 windows. After the second window, preparations were imaged during stimulation of
691 peripheral nerves (20 s per nerve). The total imaging time per preparation was 380 s.
692 Either the rostral or caudal surface of the left buccal hemiganglion was imaged. The
693 position of the objective was adjusted so that the center portion of the hemiganglion was
694 visible. Approximately 80% of the total surface area was visible on each preparation. The
695 focal plane was set to the region with the greatest number of neurons. Neurons in the
696 ventral cluster, as well as B1 and B2 when imaging the caudal surface, were consistently
697 in the field of view. However, neurons close to the edges of the field of view may not have
698 been captured in all preparations (e.g., B4/5, B8a/b, dorsal portions of the sensory
699 cluster). The position of the ganglion was reasonably consistent across experiments. In
700 addition, we accounted for variations by approximating the orientation and offset of both
701 the ventral cluster and the entire ganglion, and then aligning each recording accordingly,
702 as previously described (Neveu et al. 2017).

703 *Data processing*

704 VSD data were processed in a similar manner to that described elsewhere (Neveu
705 et al., 2017; Costa et al., 2021). Briefly, regions of interest were drawn around the soma
706 of each neuron, and the light intensity was averaged across pixels within the region for
707 each time point. Traces for each cell were taken as the change in light intensity relative
708 to baseline (i.e., $\Delta I/I$), where baseline was defined as an average of the first 10 frames
709 after shutter opening. Traces were passed through a bandpass butterworth filter (Fpass1
710 = 15 Hz, Fstop1 = 0.1 Hz, Fpass2 = 140 Hz, Fstop2 = 0.5 kHz, Apass = 0.1, Astop1 = 60,
711 Astop2 = 60).

712 Principal component analysis (PCA) was used to isolate and remove correlated
713 noise, such as that associated with movement. PCA extracts a set of components from
714 the data that can be ordered by the amount of variance-covariance in the data explained

715 by each component. If some components consist primarily of noise, the data can be
716 reconstructed without those components to improve signal-to-noise ratio. At the
717 millisecond timescale, most of the correlation between the traces of individual neurons
718 was due to noise that affected many neurons simultaneously, such as tissue movement,
719 vibrations, and fluctuations in illumination. This was the case because the amplitude of
720 RH-155 signals is very small (i.e., in the order of 1×10^{-4} $\Delta I/I$), and, importantly, because
721 action potentials in *Aplysia* are not correlated at the millisecond scale during spontaneous
722 BMP generation. Note that this is different from the correlation between firing rates
723 examined throughout this paper, which is on the scale of seconds. Thus, PCA was
724 performed on the traces from all neurons in a preparation, removed the top n components
725 accounting for 85% of the variation, and reconstructed the data. Upon visual inspection
726 of signal quality this threshold consistently reduced noise without signal decrement.

727 Spike detection was performed by the algorithm described in Neveu et al. (2017).
728 Briefly, spikes were detected in a neuron when a downward deflection in the VSD trace
729 exceeded 2.75 times the standard deviation of the trace and the peak of this downward
730 deflection was followed after 7 ms by an upward deflection in excess of 3.25 times the
731 standard deviation. The re-arm window for spike detection was set to 22.5 ms.

732 *Feature extraction*

733 *Position* and *size* of a neuron were determined based on the hand-drawn kernels
734 overlying individual neurons in a pixel coordinate of the original data (128 × 128 pixels).
735 The position of a neuron was defined as the *x* and *y* coordinates of the centroid of the
736 pixels included in the kernel. The size was defined as the total number of pixels of the
737 kernel. A small subset of neurons was located on the edge of the camera sensor, and
738 thus a part of their cell bodies was not within the field-of-view. No adjustment to size or
739 position was made to account for this.

740 All feature parameters determined from the VSD imaging of BMP activity were
741 based on the spike timing data obtained from the basic data processing described in the
742 preceding subsection. The data from two imaging windows (see *Voltage-sensitive dye*
743 *(VSD) imaging*) were concatenated. *Phase preference* features (*protraction*, *retraction*,
744 and *post-retraction*) were defined based on a simple firing rate during each of the BMP

745 phases. The number of spikes during the phase of interest and the duration of phase
746 were summed across all the occurrences of BMPs. The ratio of the summed spike counts
747 over the summed duration was considered the firing rate. *Phase preference* is defined as
748 a relative firing rate that is normalized to the highest firing rate across all neurons for a
749 given BMP phase of a given animal.

750 The properties of burst-like activity were used to obtain additional features. For this
751 purpose, the burst detection algorithm described in Neveu et al. (2017) was used. Briefly,
752 bursts were identified whenever 3 spikes occurred with ≤400 ms interspike interval, and
753 when the total firing rate within bursts was significantly different from the firing rate outside
754 of bursts. Neurons were assigned true for the binary feature *bursting* if they displayed
755 burst-like activity, and false otherwise. *Frequency* was defined as the overall firing rate
756 within burst occurring during BMPs for a given neuron, regardless of phase. The temporal
757 properties of burst-like activities were measured after normalizing all time points during a
758 given BMP phase to the duration of that phase. This approach allowed for the relative
759 timing of bursts to be captured, regardless of variability in the duration of phases and
760 BMPs. *Start time* was defined as the time elapsed between BMP onset and onset of the
761 first burst for each neuron. *Duration* was defined as the sum of the durations of all bursts
762 occurring during BMPs for a given neuron.

763 Feature parameters from the nerve stimulation experiments were based on
764 normalized kernel time courses (ΔI/I) that were not temporally filtered or denoised
765 because processing would significantly alter the waveform of response. At first, a
766 stimulus-triggered average of response was calculated for combination of neuron and
767 stimulated nerve. The VSD time course was super-sampled 10 times by replacing each
768 data point with 10 data points of the identical value. The time points of electrical shock
769 were extracted from the nerve recording and corresponding time points were found in the
770 super-sampled VSD time course. VSD data of a time-window from -100 ms to +500 ms
771 of stimulus was extracted for each occurrence of electrical stimulus and then their mean
772 time courses were calculated. In each averaged time course, drifting of baseline was
773 corrected by subtracting the mean across a time window from -20 to 0 ms from all data
774 points. The amplitude of response was defined as the integral of ΔI/I in a time window

from 0 to 25 ms. Although this time window was potentially too short for a subset of long-lasting responses, the contribution of baseline drift became detrimental when longer time windows were considered.

The feature parameters were also calculated from the half-split data to assess their discriminability (see the next subsection). Data from spontaneous activity data were split into the odd number and even number occurrences of BMP after pooling the two trials. Data of nerve-stimulation experiment were split into the odd and even number the delivery of electrical stimulation. No half-split data were considered for the position and size parameters as they were unchanging throughout the experiment.

Feature discriminability

The calculation of the discriminability index was done by dividing the data within a single experiment into two separate trials and comparing the neuron in one trial to itself, as well as to the most similar non-self neuron, in the other trial. The comparisons were performed by applying the whitening transform to the entire feature-space and then considering each feature as an independent dimension in an *F*-dimensional space. Each neuron, then, could be represented simply as a vector in this space and comparing two neurons in this space could be done by computing the *2-norm* of the vector distance between them. Thus, the *discriminability* of a given neuron *i* in feature-space *f* could be given by the following:

$$d_i^f = -log\left(\sum_{f1,f2\in f} \frac{\|n_i^{f1} - n_i^{f2}\|_2}{min_{j\neq 1}\|n_i^{f1} - n_j^{f2}\|_2}\right),$$

where *f1* and *f2* represent two trials within the same subset of features represented by *f*. The parenthetical expression represents the comparison of a neuron's self-similarity between the two trials to its most similar non-self neighbor in the feature-space. By taking the negative logarithm of this fraction, positive values are assigned to self-similar neurons

and negative values to non-self-similar ones. For a neuron *i*, if this value was positive, the neuron was said to be *discriminable* in this feature-space.

The subset of features that was most beneficial for identifying neurons across experiments should maximize the number of discriminable neurons. The total *feature-space discriminability* was given by the following expression:

$$D^f = \sum_{i=1}^{N} H(d_i^f),$$

where *H(x)* represents the Heaviside step function, used to convert positive discriminabilities into ones, which could then be tallied up to represent the total discriminability of feature-space *f*. Consequently, the feature-space is maximally informative when *D* is maximized.

To determine the optimal subset of features to maximize the feature-space discriminability, at first, a subtractive assessment of discriminability was employed: starting with the full feature set, each feature was removed one-by-one and discriminability was reassessed. If discriminability decreased with the removal, the feature was considered informative and kept in the feature set. Otherwise, the feature was considered not helpful and removed. Next, because how informative a feature is may be dependent on the redundancy of information with other features, the once-removed features were added back one-by-one and discriminability was reassessed. If the added feature increased discriminability, it was retained in the feature space.

Compared to the use of the discriminability index by Frady et al. (2016), there was a significant departure in the present study. Only functional features, but not spatial ones, were used for assessment because half-split data is unavailable for the spatial features. Although previously this was addressed by intentionally adding noise to simulate biological variation (Frady et al. 2016), the amount of added noise directly impacts the

discriminability score. Therefore, in this study, the analysis of discriminability was rather focused on the functional features with the premise that spatial features are informative.

Pairwise matching algorithm

The pairwise matching of neurons between experiments were based on the optimized feature-space. At first, the whitening transform was applied to the entire optimized feature-space for all experiments simultaneously. This transform set all the feature-space covariance matrix to the identity matrix, and normalized the values of the features, which had varying magnitudes and scales depending on the respective features.

Each neuron in one experiment was compared to all neurons in another by considering the distance of feature vectors between them. The vector distance was then converted to the matching strength, which takes into account the uniqueness of match and is defined as follows:

$$S(i,j) = \sqrt{\frac{e^{-D(i,j)}}{\sum_{i=1}^{I} e^{-D(i,j)}}},$$

where *I* represents the set of neurons in a given experiment being compared to neuron *j* in the other and neuron *i* is the neuron of interest. This expression, therefore, ranges from 0, where the distance *D* between the two neurons of interest is infinite, to 1, where *D* is 0 and all other distances to neuron *j* are infinite, meaning neuron *i* is uniquely and strongly matched to neuron *j*.

Matching pairs were determined through the Kuhn-Munkres assignment algorithm (Kuhn, 1955; also referred to as the *Hungarian method*), which enabled the combinatorial optimization, maximizing the overall strength of matches while accepting the presence of pairs with non-highest match strength. The neuron-to-neuron matches were further optimized for interanimal variability through a skewing of the feature-space of interest was performed, where the magnitude of the distance vectors between these neurons was

calculated similarly to before; although the vectors representing each neuron now had a weight matrix assigned to it, as given by the following:

$$D(i,j) = \|W_I F(i) - W_J F(j)\|_2.$$

As illustrated by the equation, the weight matrices are defined per experiment. To find weight matrices W_I and W_J, a subset of matched neuron pairs, whose match strength was above the 95th percentile among all matches between the two experiments, were used as the basis matches. Then W_I and W_J were determined such that they minimized the magnitude of the vector distance between the basis matches. Finally, the process of pairwise matching was then repeated, this time using the skewed feature-space for the determination of neuron matching.

Cross-animal evaluation of pairwise matching

The results of pairwise matching was further analyzed regarding their consistency across multiple animals. Specifically, groups of neurons satisfying the following criterion were sought: every member in the group of four neurons was matched to all three other members of the group in the pairwise match (i.e., complete four-way match). Then, groups of four neurons that share the same member neurons were merged with tolerating that a subset of neuron pairs in the merged group are not matched in pairwise matching.

For a given neuron in the entire dataset (seed neuron), all its pairwise-matched neurons were identified (from 6 other subjects in the caudal dataset or 5 subjects in the rostral dataset, unless matches are missing due to the unequal neuron numbers between subjects). Next, for a given pair of the seed neuron and its directly-matched neuron, their pairwise counterparts in the remaining subjects were identified and kept only if they were the same. If more than two neurons were kept as the shared counterparts of the seed and its direct-match, every possible pair among the kept neurons was listed and asked if they were also matched to each other in the pairwise matching. If matched, the pair and the seed neuron and the seed's direct-match were saved as a complete four-way match.

These processes were repeated for every neuron in the dataset as the seed neuron. From the resulted list of complete four-way matches, redundant entries were removed and then entries sharing the same neuron(s) were merged in a recursive manner. In case a merged group contained two neurons from the same subject, both of them were removed. The final results (i.e., a list of successful groups) were manually inspected for additional irregularities (none was detected).

Cyclic matching

After performing the skewing of the feature-space as part of pairwise matching, the neuron-to-neuron match strength was computed between all combinations of neurons for all possible pairs of experiments. For a given neuron in one experiment, every neuron from the experiments to be compared were ranked based on their match strengths. Such preference ranks were determined for every neuron in the dataset for every possible experiment to be paired.

The families of neurons with cyclic matching preferences was identified based on Hofbauer (2016) (Fig. 6A). Briefly, the order of experiment in the matching cycle was defined at first by random assignment. Starting with the first experiment in the cyclic order, the neurons in the first experiment were each matched to neurons in the second experiment as in the pairwise matching (see above). Each of these newly added neurons was matched to neurons in the next experiment, until the last experiment. For the neuron in the last experiment, the neurons to be matched in the first experiment had been already determined (i.e., the first neuron in the family) although it was not necessarily the appropriate match if the same matching process was performed. Therefore, the actual preference rank of the last neuron to the first neuron among the neurons in the first experiment was identified based on their similarities in the feature-space. The families of matches that have the best last-to-first preference rank were considered most content (highest contentness) and removed from the pool. Then the preference ranks of the neurons in the remaining matching series were updated and the same process was performed iteratively, until no more neurons remained in the experiment with the fewest neurons.

For copresence analysis (Figure 6B), the above process of cyclic matching was repeated 100 times with different orders of experiments, which were randomly permuted with no identical orders allowed. One neuron in the dataset was picked as the reference neuron, and for every neuron from every experiment except the one that includes the reference neuron, the number of runs in which the neuron of interest and the reference neuron were placed in the same family was counted and termed copresence count. Because the number of neurons in an experiment can be larger than the number of families, it is possible that the reference neuron is not placed in any of the families. The number of runs in which the reference neuron is placed in any of the families is termed appearance count, and this value sets the upper boundary of copresence count for a given reference neuron. The analysis of copresence count was performed for every neuron in the dataset as the reference neuron.

Feature skewing

Skewing of the feature-space is a core aspect of the functional neurocartography framework (Frady et al., 2016). Briefly, the algorithm, termed weighted correspondence minimization (WCM), finds a transform of the feature-space that minimizes the distance among a set of selected matches between neurons. The WCM algorithm was not modified. Instead, an approach was developed to automate selection of matches to be optimized by the WCM transform. This approach, termed cyclic skewing, was based on the copresence profiles obtained from running multiple permutations of the cyclic matching algorithm (described in the previous section). Target neurons whose copresence count proportion relative to a reference neuron surpassed a given threshold were labeled “major partners”, i.e., neurons that consistently belonged to the same family as the reference neuron. These major partners were taken as the selected matches and used as input to the WCM algorithm, which, therefore, sought a transform of the feature-space that minimized the distances among major partners. The quality of the resulting feature-space was assessed by the sparseness metric

$$sparseness = \frac{\ell_2}{\ell_1}$$

where ℓ_p is the p-norm of the copresence profile vector. A sparse vector has only a few non-zero dimensions, whereas a non-sparse vector has many non-zero dimensions. Thus, both the ℓ_1 norm (i.e., the modulus) and the ℓ_2 norm (i.e., the Euclidean distance from the origin) increase as sparseness decreases, but the ℓ_1 norm does so at a faster rate. However, either norm has the disadvantage of being scale-dependent. In the particular case of the copresence profile, reducing the appearances of a reference neuron would lead to lower ℓ_1 and ℓ_2 norms of the copresence vector, implying an increase in sparseness without a clear improvement in performance. Conversely, the ratio between the norms offer a scale-invariant alternative (Krishnan et al., 2011; Yin et al., 2014). The ratio will only imply an increase in sparseness when the distribution of copresence counts for a given reference neuron converges on fewer partner neurons, which indicates that matches are more consistent and less ambiguous across runs. Thus, this sparseness metric was used to compare the unskewed feature-space with the skewed feature-spaces using a range of copresence proportion thresholds (Fig. 7).

Identification and characterization of canonical neurons

Based on the copresence counts, putatively homologous neurons were grouped through the following procedure. To obtain the copresence counts used in this process, 100 runs of cyclic matching were repeated 10 times and mean copresence counts were calculated across the repeats for each pair of the reference neurons and the neuron of interest. Then for a given reference neuron N_1 and neurons in the experiment under comparison, the neuron with the highest copresence count was identified as N_2 and its uniqueness index (UI) is defined as follows,

$$UI = \begin{cases} \dfrac{CC_{best} - CC_{second-best}}{CC_{best} + CC_{second-best}}, & \text{neurons with highest copresence counts} \\ \dfrac{CC_{non-best} - CC_{best}}{CC_{non-best} + CC_{best}}, & \text{other neurons} \end{cases}$$

where CC_{best} is the copresence count of N_2 and $CC_{second\text{-}best}$ is that of the neuron with the second-highest count of the same experiment after N_2. (The definition of UI is extended for neurons not with the highest count and defined by the second equation, where $CC_{non\text{-}}$

965 $_{best}$ is the copresence count of that neuron.) When UI was above 0.5, N_2 was set as the
966 new reference neuron and it was tested whether N_1 showed the highest copresence count
967 in the experiment under comparison with UI above 0.5. If true, N_1 and N_2 were considered
968 as an established pair of neurons. From the UI equation it follows that a value of 0.5 is
969 equivalent to a copresence count that is three times higher for the best neuron than the
970 count of the second-best. This value was chosen as a threshold to have minimal false
971 positives considering the standard error of the mean copresence counts. Next, for each
972 neuron that formed an established pair, all established pairs including that neuron were
973 gathered as a preliminary group. For the preliminary groups, if one is identical to or a
974 subset of another preliminary group, they were integrated into a single preliminary group.
975 In case a single preliminary group contained two member neurons from the same
976 experiment at this point, both of them were removed. Finally, if two preliminary groups
977 shared a subset of members but each also had its unique member(s) (e.g., U_1 from one
978 preliminary group and U_2 from another, it was tested whether U_1 made an established
979 match with a different neuron from the experiment including U_2, or vice versa). If neither
980 is true (i.e., there was no explicit conterevidence), they were allowed to be merged as a
981 single group. If either (or both) is true, U_1 and U_2 were removed and only shared members
982 were kept in the merged preliminary group. Preliminary groups that had four or more
983 member neurons at this point were defined as the groups of putatively homologous
984 neurons.

985 For each group of putatively homologous neurons based on cyclic matching, all
986 pre-skewed feature parameters of member neurons were retrieved and the median
987 across member neurons were calculated for each feature. The resulted set of median
988 feature parameters were considered as the features representing the group of
989 homologous neurons (i.e., a canonical neuron).

990 *Code and data availability*

991 Code and data will be deposited to public repositories following peer-review.

992 **REFERENCES**

993 Åberg KM, Alm E, Torgrip RJO (2009) The correspondence problem for metabonomics
994 datasets. Anal Bioanal Chem 394:151–162 doi: 10.1007/s00216-009-2628-9.

995 Abrahao KP, Lovinger DM (2018) Classification of GABAergic neuron subtypes from the
996 globus pallidus using wild-type and transgenic mice. J Physiol 596:4219–4235. doi:
997 10.1113/JP276079

998 Baxter DA, Byrne JH (2006) Feeding behavior of *Aplysia*: A model system for comparing
999 cellular mechanisms of classical and operant conditioning. Learn Mem 13:669–680
1000 doi: 10.1101/lm.339206

1001 Björklund A, Dunnett SB (2007) Dopamine neuron systems in the brain: an update.
1002 Trends Neurosci 30:194–202. doi: 10.1016/j.tins.2007.03.006

1003 Byrne JH ed. (2019) The Oxford Handbook of Invertebrate Neurobiology. New York:
1004 Oxford University Press. doi: 10.1093/oxfordhb/9780190456757.001.0001

1005 Church PJ, Cohen KP, Scott ML, Kirk MD (1991) Peptidergic motoneurons in the buccal
1006 ganglia of *Aplysia californica*: Immunocytochemical, morphological, and physiological
1007 characterizations. J Comp Physiol A 168:323–336. doi: 10.1007/BF00198352.

1008 Costa RM, Baxter DA, Byrne JH (2020) Computational model of the distributed
1009 representation of operant reward memory: combinatoric engagement of intrinsic and
1010 synaptic plasticity mechanisms. Learn Mem 27:236–249. doi: 10.1101/lm.051367.120

1011 Costa RM, Baxter DA, and Byrne JH (2021) Neuronal population activity dynamics reveal
1012 a low-dimensional signature of operant learning. bioRxiv: 2021.12.06.471434

1013 Cropper EC, Evans CG, Hurwitz I, Jing J, Proekt A, Romero A, Rosen SC (2004) Feeding
1014 neural networks in the mollusc *Aplysia*. NeuroSignals 13:70–86. doi:
1015 10.1159/000076159

1016 Cropper EC, Kupfermann I, Weiss KR (1990) Differential firing patterns of the peptide-
1017 containing cholinergic motor neurons B15 and B16 during feeding behavior in *Aplysia*.
1018 Brain Res 522:176–179. doi: 10.1016/0006-8993(90)91598-B

1019 Dembrow NC, Jing J, Proekt A, Romero A, Vilim FS, Cropper EC, Weiss KR (2003) A
1020 newly identified buccal interneuron initiates and modulates feeding motor programs in
1021 *Aplysia*. J Neurophysiol 90:2190–2204. doi: 10.1152/jn.00173.2003

1022 Elliott CJH, Susswein AJ (2002) Comparative neuroethology of feeding control in
1023 molluscs. J Exp Biol 205:877–896. doi: 10.1242/jeb.205.7.877

1024 Evans CG, Cropper EC (1998) Proprioceptive input to feeding motor programs in *Aplysia*.
1025 J Neurosci 18:8016–8031. doi: 10.1523/JNEUROSCI.18-19-08016.1998

1026 Frady EP, Kapoor A, Horvitz E, Kristan WB (2016) Scalable semisupervised functional
1027 neurocartography reveals canonical neurons in behavioral networks. Neural Comput
1028 28:1453–1497. doi: 10.1162/NECO_a_00852

1029 Frady EP, Kristan WB (2015) The Imaging computational microscope. arXiv: 1502.07009

1030 Gardner D (1971) Bilateral Symmetry and Interneuronal Organization in the buccal
1031 ganglia of *Aplysia*. Science 173:550–553. doi: 10.1126/science.173.3996.550

1032 Hassanien AE, Abraham A, Peters JF, Schaefer G, Henry C (2009) Rough Sets and
1033 Near Sets in Medical Imaging: A Review. IEEE Trans Inf Technol Biomed 13:955–968.
1034 doi: 10.1109/TITB.2009.2017017

1035 Hernández VM, Hegeman DJ, Cui Q, Kelver DA, Fiske MP, Glajch KE, Pitt JE, Huang
1036 TY, Justice NJ, Savio Chan C (2015) Parvalbumin+ neurons and Npas1+ neurons are
1037 distinct neuron classes in the mouse external globus pallidus. J Neurosci 35:11830–
1038 11847. doi: 10.1523/JNEUROSCI.4672-14.2015

1039 Hofbauer J (2016) D-dimensional stable matching with cyclic preferences. Math Soc Sci
1040 82:72–76. doi: 10.1016/j.mathsocsci.2016.04.006

1041 Jing J, Weiss KR (2001) Neural mechanisms of motor program switching in *Aplysia*. J
1042 Neurosci 21:7349–7362. doi: 10.1523/JNEUROSCI.21-18-07349.2001

1043 Kabotyanski EA, Baxter DA, Byrne JH (1998) Identification and characterization of
1044 catecholaminergic neuron B65, which initiates and modifies patterned activity in the
1045 buccal ganglia of *Aplysia*. J Neurophysiol 79:605–621. doi: 10.1152/jn.1998.79.2.605

1046 Krishnan D, Tay T, Fergus R (2011) Blind deconvolution using a normalized sparsity
1047 measure. In: Proceedings of the IEEE Computer Society Conference on Computer
1048 Vision and Pattern Recognition, pp 233–240. doi: 10.1109/CVPR.2011.5995521

1049 Kuhn HW (1955) The Hungarian method for the assignment problem. Nav Res Logist Q
1050 2:83–97. doi: 10.1002/nav.3800020109

1051 Mallet N, Micklem BR, Henny P, Brown MT, Williams C, Bolam JP, Nakamura KC, Magill
1052 PJ (2012) Dichotomous organization of the external globus pallidus. Neuron 74:1075–
1053 1086. doi: 10.1016/j.neuron.2012.04.027

1054 McManus JM, Lu H, Cullins MJ, Chiel HJ (2014) Differential activation of an identified
1055 motor neuron and neuromodulation provide *Aplysia*'s retractor muscle an additional
1056 function. J Neurophysiol 112:778–791. 10.1152/jn.00148.2014

1057 Morton DW, Chiel HJ (1993a) In vivo buccal nerve activity that distinguishes ingestion
1058 from rejection can be used to predict behavioral transitions in *Aplysia*. J Comp Physiol
1059 A 172:17–32. doi:10.1007/BF00214712

1060 Morton DW, Chiel HJ (1993b) The timing of activity in motor neurons that produce radula
1061 movements distinguishes ingestion from rejection in *Aplysia*. J Comp Physiol A
1062 173:519–536. doi: 10.1007/BF00197761

1063 Nargeot R, Baxter DA, Patterson GW, Byrne JH (1999) Dopaminergic synapses mediate
1064 neuronal changes in an analogue of operant conditioning. J Neurophysiol 81:1983–
1065 1987. doi: 10.1152/jn.1999.81.4.1983

1066 Neveu CL, Costa RM, Homma R, Nagayama S, Baxter DA, Byrne JH (2017) Unique
1067 configurations of compression and truncation of neuronal activity underlie L-DOPA–
1068 induced selection of motor patterns in *Aplysia*. eNeuro 4:ENEURO.0206-17.2017. doi:
1069 10.1523/ENEURO.0206-17.2017

1070 Plummer MR, Kirk MD (1990) Premotor neurons B51 and B52 in the buccal ganglia of
1071 *Aplysia californica*: Synaptic connections, effects on ongoing motor rhythms, and
1072 peptide modulation. J Neurophysiol 63:539–558. doi: 10.1152/jn.1990.63.3.539

1073 Scott ML, Govind CK, Kirk MD (1991) Neuromuscular organization of the buccal system
1074 in *Aplysia californica*. J Comp Neurol 312:207–222. doi: 10.1002/cne.903120204

Susswein AJ, Byrne JH (1988) Identification and characterization of neurons initiating patterned neural activity in the buccal ganglia of *Aplysia*. J Neurosci 8:2049–2061. 10.1523/jneurosci.08-06-02049.1988

Tiklová K, Björklund ÅK, Lahti L, Fiorenzano A, Nolbrant S, Gillberg L, Volakakis N, Yokota C, Hilscher MM, Hauling T, Holmström F, Joodmardi E, Nilsson M, Parmar M, Perlmann T (2019) Single-cell RNA sequencing reveals midbrain dopamine neuron diversity emerging during mouse brain development. Nat Commun 10. doi: 10.1038/s41467-019-08453-1

Yendiki A, Reuter M, Wilkens P, Rosas HD, Fischl B (2016) Joint reconstruction of white-matter pathways from longitudinal diffusion MRI data with anatomical priors. Neuroimage 127:277–286. doi: 10.1016/j.neuroimage.2015.12.003

Yin P, Esser E, Xin J (2014) Ratio and difference of ℓ_1 and ℓ_2 norms and sparse representation with coherent dictionaries. Commun Inf Syst 14:87–109. doi: 10.4310/cis.2014.v14.n2.a2